The small-scale structure of the high-latitude molecular cloud toward HD 210121

Gredel, R.; Dishoeck, E.F. van; Black, J.H.; Vries, C.P. de

Astron. Astrophys. 257, 245–264 (1992)

ASTRONOMY AND ASTROPHYSICS

The structure of the high-latitude molecular cloud toward HD 210121*

Roland Gredel[1,2], Ewine F. van Dishoeck[3,4], Cor P. de Vries[5], and John H. Black[4,6]

[1] European Southern Observatory, La Silla, Chile
[2] I. Physikalisches Institut der Universität zu Köln, Zülpicher Str. 77, W-5000 Köln 41, Federal Republic of Germany
[3] Div. of Geological and Planetary Sciences, Caltech 170–25, Pasadena CA 91125, USA
[4] Sterrewacht Leiden, P.O. Box 9513, NL-2300 RA Leiden, The Netherlands
[5] Laboratory for Space Research, P.O. Box 9504, NL-2300 RA Leiden, The Netherlands
[6] Steward Observatory, University of Arizona, Tucson, AZ 85721, USA

Received December 3, 1990; accepted September 12, 1991

Abstract. Millimetre emission and optical absorption line observations of the high-latitude cloud toward the star HD 210121 are reported. The cloud was mapped in the $J=1\rightarrow0$ transition of ^{12}CO with the 15 m Swedish-ESO Submillimetre Telescope (SEST) at 1′ spacing. The emission is characterized by a number of distinct peaks embedded in widespread, low-level emission over an area of one square degree, which corresponds to a diameter of 2.6 parsec at the estimated distance to the cloud of 150 pc. A fully-sampled high signal-to-noise map was made over a $3'\times3'$ region around the star, which allows a study of the structure on smaller scales. Limited maps in the ^{13}CO $J=1\rightarrow0$ line were obtained in regions of local ^{12}CO maxima, where the structure may change on spatial scales of less than 0.1 pc. The ^{13}CO emission was found to have a smaller spatial extent and a steeper gradient toward the boundaries of the clumps than the ^{12}CO emission. The velocity gradient across the cloud is small, ≤1 km s^{-1} over 2.6 pc. The optical absorption line observations toward HD 210121 allow an independent determination of the H_2 column density along the line of sight against which the CO/H_2 conversion factors can be calibrated. It is shown that the standard analysis of the ^{13}CO emission in dense, thick clouds does not apply to this more tenuous cloud. The optical absorption lines of C_2 and CN detected toward HD 210121 can be used to estimate the physical conditions in the cloud. The C_2 excitation suggests a low temperature, $T\leq20$ K, and a rather low, but uncertain density $n_H\approx500$–1000 cm^{-3}. The CN excitation derived from the absorption lines, combined with sensitive searches for the CN millimetre emission line, indicates densities $n_H\approx1500$–2500 cm^{-3}. An analysis of the CO rotational excitation gives densities $n_H\approx2000$–5000 cm^{-3}. Little evidence is found for large density variations between various positions in the cloud from these diagnostics. Millimetre lines of other molecules such as HCN, HCO^+ and C_3H_2 were searched for, but not detected. Most of the observed molecular abundances and upper limits can be understood in models with densities $n_H\approx500$–5000 cm^{-3}, and a low incident ultraviolet radiation field. The observed $^{12}CO/^{13}CO$ ratios can be reproduced in models in which the temperature is sufficiently low. The molecular column densities found in this cloud are consistent with those measured in diffuse and translucent molecular clouds. The effects of small-scale structure and low filling factors on the analysis are discussed. The cloud lies in the interesting regime in which the abundance of CO starts to become significant, but in which most carbon is still in atomic form. It is pointed out that in this regime, small fluctuations in physical parameters can lead to large variations in observable CO line intensity, thereby accentuating the structure seen in the CO map. As a general conclusion, it is not trivial to distinguish density variations from variations in other properties such as total hydrogen column density, strength of the ultraviolet radiation field, extinction properties of grains or carbon depletion factor.

Key words: interstellar medium: molecules – clouds: HD 210121 – radio lines: molecular

1. Introduction

The first systematic search for ^{12}CO $J=1\rightarrow0$ emission at latitudes $|b|\geq20°$ was performed by Blitz et al. (1984), who detected a number of localized regions of CO emission which are now referred to as high-latitude molecular clouds. The clouds may be distinguished from the opaque, dark clouds at high galactic latitudes listed in Lynds' (1962) catalogue by their low visual extinction of typically $A_V^{tot}=1$–2 mag (Magnani & de Vries 1986). The clouds detected in CO are local and appear at an average distance of $D\approx100$ pc (Magnani & de Vries 1986; Hobbs et al. 1986, 1988). They are associated with "cirrus" emission reported from IRAS observations at 100 μm (de Vries & Le Poole 1985; Weiland et al. 1986; de Vries et al. 1987) and with atomic H I emission (Goerigk et al. 1983; Mebold et al. 1985). The IRAS database has subsequently been used to identify a larger collection of high-latitude diffuse molecular clouds (Désert et al. 1988), of which the Magnani et al. (1985) sample is only a subset.

Despite their low visual extinction, the clouds have relatively high abundances of CO (Magnani et al. 1985; Keto & Myers 1986) compared with, for example, the classical diffuse clouds studied by ultraviolet absorption lines with the *Copernicus* satellite. Other molecules that have been detected in high-latitude clouds by their millimetre emission lines include OH and H_2CO

Send offprint requests to: E.F. van Dishoeck, Leiden
* Based on observations collected at the European Southern Observatory, La Silla, Chile

(Magnani et al. 1988; Heithausen et al. 1987; Magnani & Siskind 1990), CH (Magnani et al. 1989), C_3H_2 (Turner et al. 1989), CS (Drdla et al. 1989), and NH_3 (Mebold et al. 1987; Stacy et al. 1989). Most of the clouds in which molecules have been observed are poorly characterized in terms of physical parameters and total H_2 column density, however, so that the determination of the abundances is rather uncertain. In addition, the CO maps of high-latitude clouds are often significantly undersampled, with effective spacings of 2–10′. Only a few clouds have been mapped at higher angular resolution (e.g. Falgarone & Pèrault 1988; Pound et al. 1990). The clouds are generally several square degrees in extent, and show a highly inhomogeneous and filamentary structure down to the actual resolution of the telescopes.

Because the high-latitude clouds are thin, they are also amenable to optical absorption line studies, provided that a suitable background star can be found. Atomic Na I lines toward stars located behind known high-latitude clouds were observed by Hobbs et al. (1986, 1988), and were used to place more stringent constraints on the distances to individual clouds. Absorption lines of interstellar CH and CH^+ have been discovered by de Vries & van Dishoeck (1988), Welty et al. (1989), and Penprase et al. (1990).

In many aspects, the high-latitude clouds are very similar to the translucent clouds studied by van Dishoeck & Black (1989). The "tiny little clouds" discovered by Knapp & Bowers (1988) probably belong in the same category on empirical grounds, even if not of similar origin. Translucent clouds are defined as molecular clouds with visual extinctions in the range $A_V^{tot} \approx 1$–5 mag. Their most interesting chemical property is that they lie in the region of parameter space where carbon is transformed from predominantly C^+ to CO (van Dishoeck & Black 1988). It is becoming apparent that the high-latitude clouds actually span a wide range of cases. On the one hand, there are high-latitude clouds which show peak CO antenna temperatures approaching those of classical dark clouds such as L134 N and TMC-1, and in which molecules such as C_3H_2 and NH_3 are detected. Examples are MBM 12 (Pound et al. 1990), MBM 16, MBM 20, MBM 21 and MBM 40 (Magnani et al. 1988; Turner et al. 1989; Stacy et al. 1989). The cores of these clouds surely have visual extinctions of more than three magnitudes in localized places, and most carbon has been transformed into CO. On the other hand are the diffuse molecular clouds listed by Désert et al. (1988), which show in many cases no CO emission at the level of $T_R^* \approx 0.2$ K (Blitz et al. 1990). Nearly 90% of the high-latitude molecular clouds appear to fall into this category, and the total visual extinctions (including that contributed by the atomic component) are less than 1 magnitude. These clouds are similar to the classical diffuse clouds studied with the *Copernicus* satellite such as the ζ Oph cloud, in which most carbon is observed to exist in the form of C^+. The majority of the original MBM clouds observed in CO lie presumably in the important intermediate regime where CO just starts to become significant. A more detailed study of the physical and chemical structure of clouds in this class is certainly warranted.

We have therefore undertaken a detailed study of the high-latitude cloud toward HD 210121 discovered by de Vries & van Dishoeck (1988) on the basis of the IRAS 100 μm data, and listed as cloud nr. 80 by Désert et al. (1988). This cloud is better suited for a thorough investigation than many other clouds in the sample for several reasons. First, it has at least one bright, early-type background star against which absorption lines can be measured: HD 210121. This line of sight shows the strongest molecular absorption lines detected so far in a high-latitude cloud. The optical data can be used to provide independent information on the total H_2 column density along the line of sight and on other physical properties, against which the millimetre data can be calibrated. Second, its high latitude, $|b| = 44°$, ensures that it is not the outer extension of a giant molecular cloud or a dark cloud located close to the galactic plane, as is the case for some high-latitude clouds with $|b| \leq 25°$. Third, the HD 210121 cloud appears to fall nicely in the intermediate regime of clouds, in which CO is abundant, but not yet the dominant carbon-bearing species. The CO millimetre lines are therefore weak, $T_A^* \approx 1$–3 K, and only slightly saturated so that they can reveal structure on small scales. We present here detailed maps of the ^{12}CO and ^{13}CO $J = 1 \rightarrow 0$ emission at higher angular resolution (45″) than obtained for most other high-latitude clouds so far. In Sect. 2, we discuss the observational procedures. In Sects. 3.1 and 3.2, we present maps of the ^{12}CO and ^{13}CO emission. In Sects. 3.3 and 3.4, we investigate the line profiles and the velocity structure of the cloud, and in Sects. 3.5 and 3.6 we infer molecular masses and other physical parameters. The chemical structure of the cloud is discussed in Sect. 4 with reference to detailed chemical models.

2. Observations

Millimetre emission line observations were carried out in a region of approximately one square degree around the high-latitude star HD 210121 ($\alpha_{1950} = 22^h05^m36^s.1$, $\delta_{1950} = -3°46'35''.5$; $l_{II} = 56°.48$, $b_{II} = -44°.07$) with the Swedish-ESO Submillimetre Telescope (SEST) at La Silla, at an altitude of 2300 m. ^{12}CO $J = 3 \rightarrow 2$ observations at a few selected positions were made with the 10.5 m Caltech Submillimetre Observatory (CSO) at Mauna Kea (van Dishoeck et al. 1991). Optical absorption line data toward HD 210121 were obtained with the ESO 1.4 m Coudé Auxiliary Telescope (CAT) equipped with the Coudé Echelle Spectrometer (CES). In the following, we describe the observational procedures and their associated uncertainties in more detail.

2.1. *Millimetre emission line observations*

The millimetre emission line observations were obtained during several observing sessions in the period November 1988–June 1991. The characteristics of the SEST are given in Booth et al. (1989). The region around HD 210121 was extensively mapped in the $J = 1 \rightarrow 0$ ^{12}CO transition at 115.271 GHz. Restricted maps in the ^{13}CO emission at 110.201 GHz were obtained at selected positions. The spacing between individual map positions was typically 1′ for the ^{12}CO and 20″ for the ^{13}CO observations. The SEST full half power beam width (FHPBW) at 2.6 mm is 45″, so that the ^{12}CO maps are only slightly undersampled. A total of 1760 ^{12}CO and 320 ^{13}CO spectra were obtained. Spectra with relative offsets of less than 0′.1 were averaged, and the final maps were constructed from the resulting 1500 ^{12}CO and 240 ^{13}CO spectra. In addition to the ^{12}CO and ^{13}CO observations, emission lines of C_3H_2 near 85.339 GHz, HCN near 88.631 GHz, HCO^+ at 89.188 GHz, CS at 97.98 GHz, $C^{18}O$ at 109.782 GHz, and CN near 113.5 GHz were searched for at a few positions.

A dual polarization Schottky mixer was used as the frontend, with a measured total single sideband noise temperature of $T_{rec} \approx 300$ K. System temperatures above the atmosphere were

typically 600 K at 115 GHz and 450 K at the lower frequencies. Typical on-source integration times were 30 s and 100 s for the individual ^{12}CO and ^{13}CO spectra, resulting in rms noise levels of 0.35 K and 0.13 K, respectively.

A high resolution acousto-optical spectrometer (AOS), built by the millimetre astronomy group at the University of Cologne, was used as the backend. It has a band width of 86 MHz and a resolution of 43 kHz, corresponding to 0.11 km s^{-1} at 115 GHz (Zensen 1984). The Cologne AOS uses a laser diode as its light source, which during some of the observing runs caused instabilities in the frequency of the AOS output. It appeared that the current applied to the laser diode was very close to a value at which jumps occur in the emission mode of the diode. These jumps were discrete in frequency and irregular in time. They resulted in shifts of the AOS frequency scale of up to 0.15 MHz, corresponding to 0.4 km s^{-1} at 115 GHz. More regular drifts in the AOS center frequency are introduced by temperature variations in the AOS room and can amount up to two channels (86 kHz). The AOS wavelength calibration is established at the beginning of each calibration measurement through an internal frequency comb. A few spectra may, however, have an ill-defined velocity scale of up to 0.4 km s^{-1} or distorted line profiles due to jumps occurring between two integrations.

Another instrumental effect was introduced by the phase lock loop (PLL) electronics. The spectrum of the down-converted local oscillator signal shows symmetric side-lobes at an attenuation of $\approx$15 dB below the peak intensity of the signal, and additional noise structure at an attenuation of $\approx$20 dB. This particular line shape of the Gunn oscillator causes the appearance of artificial wings in the line profile of the intermediate frequency signal with an intensity of a few percent of that at the line center. At 115 GHz, these wings extend a few km s^{-1} from the line core. Therefore, any "wings" in our spectra at that level are not to be trusted.

All observations were carried out in frequency switched mode, with a frequency throw of 15 MHz in general, except for the CN observations where a throw of 40 MHz was employed. The LSR velocity of the telluric CO line was monitored carefully to avoid confusion with the observed interstellar ^{12}CO $J=1\rightarrow0$ emission. Pointing checks were carried out regularly, typically in intervals of 6 h, by observing late type stars with maser emission in the SiO $(2\rightarrow1, v'=1)$ line at 86.243 GHz. The deviations from the pointing model were found to be of the order of 5″ both in azimuth and elevation.

Calibration was achieved through the chopper-wheel method, resulting in T_A^*, the antenna temperature corrected for atmospheric attenuation and the fraction of the antenna solid angle looking at the sky (Kutner & Ulich 1981). The "chopper" main beam efficiency $\eta_{MB}^*=0.74$ and the "chopper" moon efficiency $\eta_{Moon}^*=0.91$ were derived from observations of Mars and the Moon, respectively, where $\eta_{Moon}^*=T_A^*(\text{Moon})/T_R^*(\text{Moon})$ and $\eta_{MB}^*=T_A^*/T_R(\text{MB})$. In the calculation of the main beam efficiency from the observations of Mars, a correction was made according to $T_R(\text{MB})=T_R\times[1-e^{-\ln 2\times(D/\text{FHPBW})^2}]$ where D is the disk diameter of a source not filling the main beam and FHPBW is the full width at half power of the main beam, assuming that it has a Gaussian shape. The radiation temperature of extended sources was determined from $T_R=T_A^*/\eta_{Moon}^*$ assuming that $T_R=T_R^*$. The main beam antenna temperature was defined using $T_{MB}=T_A^*/\eta_{MB}^*$. The calibration was occasionally checked by observing Orion A and IRC+10216, and was found to be consistent within 10–20%. However, comparison of the SEST CO 1–0 data with those obtained at other telescopes showed differences at selected positions of 30% or more, with the SEST data being systematically lower (e.g. van Dishoeck et al. 1991). No extra correction for this effect has been made in this work, but the uncertainty in absolute value should be kept in mind.

The submillimetre observations of the CO $J=3\rightarrow2$ line using the CSO have been described in detail by van Dishoeck et al. (1991).

2.2. *Optical absorption line observations*

Absorption lines of interstellar CH and CH^+ toward HD 210121 [$V=7.5$; $E(B-V)=0.32$] have been detected by de Vries & van Dishoeck (1988) using the 1.4 m CAT telescope with the CES. A similar instrumental set-up was used to search for interstellar CN and C_2 toward the star. Lines of CN in the $B^2\Sigma^+$–$X^2\Sigma^+$ (0,0) band around 3875 Å were observed in July 1988 and May 1990 using the short camera with the CCD detector. A search for the CN $A^2\Pi$–$X^2\Sigma^+$ (2,0) band at 7906 Å was made as well. Measurements of the C_2 $A^1\Pi_u$–$X^1\Sigma_g^+$ (2,0) lines around 8750 Å were made in August 1989 with the short camera. The detector consists of a 1024×640 pixels RCA CCD chip with a pixel size of 15 μm square (Dekker et al. 1986). At blue wavelengths, the resolving power was about $\lambda/\Delta\lambda\approx60\,000$ or 4.9 km s^{-1} in velocity units, whereas at red wavelengths, it was only $\lambda/\Delta\lambda\approx50\,000$ or 6 km s^{-1} with the short camera. Wavelength calibration was performed using a Th–Ar hollow cathode lamp as the reference. Exposure times were typically 30 min per CCD frame, with a total of 4 h for the CN observations, and 5 h for the C_2 observations. Standard lamps were used to correct for pixel to pixel sensitivity variations. The spectra were reduced with the ESO IHAP image processing system.

3. Physical properties of the cloud

The ^{12}CO $J=1\rightarrow0$ millimetre emission line toward HD 210121 shows a single component at $V_{LSR}=-6.3$ km s^{-1} (Drdla et al. 1989). This velocity is consistent with that found for the CH absorption lines toward the star, and strongly suggests that all CO emission arises from material located in front of the star (de Vries & van Dishoeck 1988). The photometric distance to the star is 210 ± 30 pc, which is thus an upper limit to the distance of the cloud. This distance could be better constrained by photometric observations of other stars in the surroundings (cf. Hobbs et al. 1986), and such work is in progress. We adopt here $D=150$ pc to the cloud. The corresponding vertical distance from the Galactic plane is $z=104$ pc. The color excess of the star, $E(B-V)=0.32$ mag, corresponds to $A_V\approx1$ mag if the standard value for the ratio of total to selective extinction $A_V/E(B-V)=3.1$ is adopted, and is consistent with the excess surface brightness at 100 μm of about 7 MJy sr^{-1}. The Na absorption lines show a weak second component at $V_{LSR}=+5$ km s^{-1}, which is not seen in the millimetre observations.

3.1. *Spatial structure of the ^{12}CO emission*

Molecular emission in the $J=1\rightarrow0$ line of ^{12}CO was detected in a region of approximately one square degree in extent (2.6 × 2.6 pc) around the star HD 210121. A contour map of the ^{12}CO $1\rightarrow0$ peak antenna temperature is presented in Fig 1a. The map was

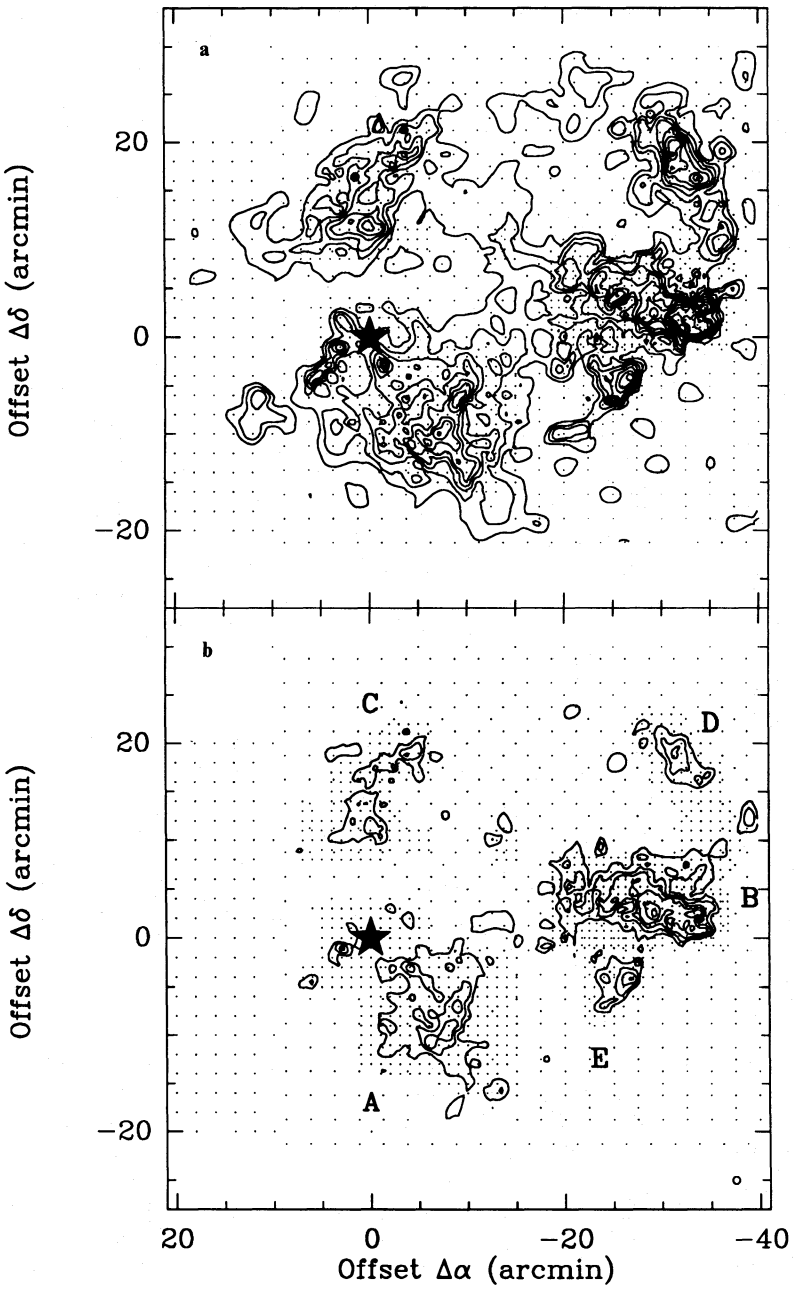

Fig. 1. a Map of the peak antenna temperature T_A^* of ^{12}CO in the HD 210121 cloud. The lowest contour is $T_A^* = 1$ K, and the increment between subsequent contours is 0.5 K. The position of HD 210121 is indicated by the star. Dots indicate the positions of the individual ^{12}CO observations. Map coordinates are given in offsets in arcmin from the stellar position. **b** Map of the velocity-integrated antenna temperature $\int T_A^* dV$ of ^{12}CO in the HD 210121 cloud. The lowest contour is set at 3 K km s^{-1} to emphasize the regions of peak CO emission, and the increment between subsequent contours is 1 K km s^{-1}. Five individual regions of ^{12}CO emission are indicated by letters A–E. The circle in the lower right corner indicates the SEST beamwidth of 45″ at 2.6 mm

constructed from parameters obtained from single Gaussians fitted to the spectra. The lowest contour drawn is $T_A^* = 1$ K and each additional level is incremented by 0.5 K.

The region around HD 210121 is characterized by extended, low-level emission with $T_A^* = 1$–2 K. Immersed in the widespread ^{12}CO emission are regions with significantly higher antenna temperatures of $T_A^* = 4$–5 K. Figure 1b shows a map of the velocity integrated antenna temperature $\int T_A^* dV$ with the low limit cutoff set at $\int T_A^* dV = 3$ K km s^{-1} to emphasize these regions. Maximum values are around $\int T_A^* dV = 8$ K km s^{-1}. The beam size of 45″ of SEST is indicated in the lower right corner. The cloud has the overall appearance of a shell-like structure, with the regions of higher antenna temperature lying at the edges of the shell. Especially in the south–west, the edge appears very sharp. In the following we distinguish the individual regions A to E as indicated in Fig. 1b.

Region A extends around and to the south–west of the direction toward HD 210121. It consists of several individual clumps with ^{12}CO intensities of $4.5 \leq \int T_A^* dV \leq 5.5$ K km s^{-1} and angular extents of a few arcmin. The ^{12}CO peak at offsets around $(-8, -10)$ was also observed in ^{13}CO. Figure 2a shows a combined map of the ^{12}CO and ^{13}CO peak antenna temperature T_A^* of a $5' \times 5'$ (0.2×0.2 pc) region. The positions of ^{13}CO observations are indicated by dots. The ^{12}CO contours range from 3.5 to 5.5 K and are incremented by 0.5 K. The lowest ^{13}CO contour is 0.75 K, and each additional contour is increased by 0.2 K. ^{13}CO emission with $T_A^* \geq 0.3$ K was detected at each position observed. The ^{12}CO and ^{13}CO maxima occur at the

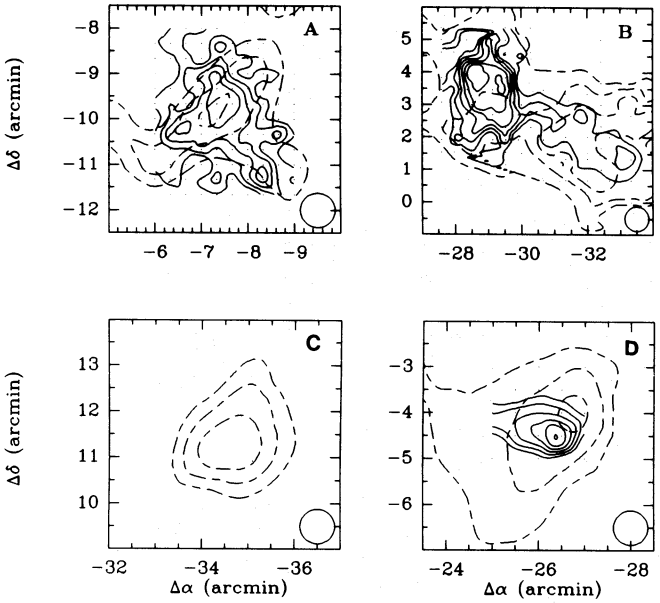

Fig. 2a–d. Map of the ^{12}CO and ^{13}CO peak antenna temperature T_A^* in Region A. The ^{12}CO contours, represented by dashed lines, range from 3.5 to 4.5 K in steps of 0.5 K. The ^{13}CO contours range from 0.75 to 1.35 K and are drawn as solid lines. Positions of ^{13}CO observations are indicated by dots. The SEST beamwidth is indicated in the lower right corner. Map of the ^{12}CO and ^{13}CO peak antenna temperature T_A^* in Region B. Symbols and notation as in Fig. 2a. The ^{12}CO contours drawn have T_A^* = 3–5 K in steps of 1 K; ^{13}CO contours start at T_A^* = 0.6 K and are incremented by 0.2 K. Map of the ^{12}CO peak antenna temperature T_A^* of the second emission component of region D at $V_{LSR} = -8$ km s^{-1}. Contour levels range from T_A^* = 1.5 K to T_A^* = 2.5 K in steps of 0.5 K. Map of the ^{12}CO and ^{13}CO peak antenna temperature T_A^* for the isolated clump of region E. The lowest contours are 2 and 0.5 K for ^{12}CO and ^{13}CO, with increments of 1 and 0.1 K, respectively. Symbols and notation as in Fig. 2a

same projected offset from the star. However, the ^{13}CO contours indicate a steeper gradient in the emission than the ^{12}CO emission: the ^{12}CO emission changes by only 20% over the map, whereas the ^{13}CO line strength changes by a factor of two over the same area. Similar effects were found by Falgarone & Pérault (1988) for part of a cloud in Ursa Major.

The ^{12}CO emission in region B shows an elongated clump with an extension of 10′ × 5′ (0.4 × 0.2 pc), and sub-structure at smaller scales. Maximum antenna temperatures are $T_A^* \approx 5$ K. Steep gradients in the emission delineate well-defined boundaries. Significant changes in T_A^* occur at spatial scales smaller than 1′. In Fig. 2b, the ^{12}CO and ^{13}CO observations in a 7′ × 7′ region around (−29, 3) are shown. The data are presented as in Fig. 2a. The lowest contours have $T_A^*(^{12}\text{CO}) = 3$ K and $T_A^*(^{13}\text{CO}) = 0.8$ K, with increments of 1 K (^{12}CO contours) and 0.2 K(^{13}CO contours). The ^{13}CO maximum is displaced from two local ^{12}CO maxima near (−29, 2.5) and (−32.5, 2). At the latter two positions, the ^{13}CO peak antenna temperature is low ($T_A^* \approx 0.6$ K) compared with values a factor of 2.5 higher at positions around (−29, 3.5). No ^{13}CO emission was detected at offsets (−32.5, 5) and (−32.5, −0.75) at the level $T_A^* \approx 0.1$ K, even though there is still significant ^{12}CO emission.

The region around position C to the north of the star is relatively free of strong ($T_A^* > 3$ K) CO emission, so it was not studied in ^{13}CO.

A small clump moving at larger negative velocities than the bulk of the CO emission in the HD 210121 cloud is seen in region D at offsets around (−35, 12). Here the ^{12}CO profile has a resolved double structure (cf. Fig. 3c). In Fig. 2c, the distribution of the second component at $V_{LSR} \approx -8$ km s^{-1} is presented. The ^{12}CO observations of this region were obtained with an integration time of 120 s, resulting in a rms noise level of 0.15 K. The ^{13}CO emission at (−35, 12) is weak but also shows the double structure. Because the average velocity of the two components is the same as that of most of the gas in the HD 210121 cloud, it is most plausible that both components are associated with the general cloud, although we cannot exclude the possibility that it is unrelated material lying along the line of sight.

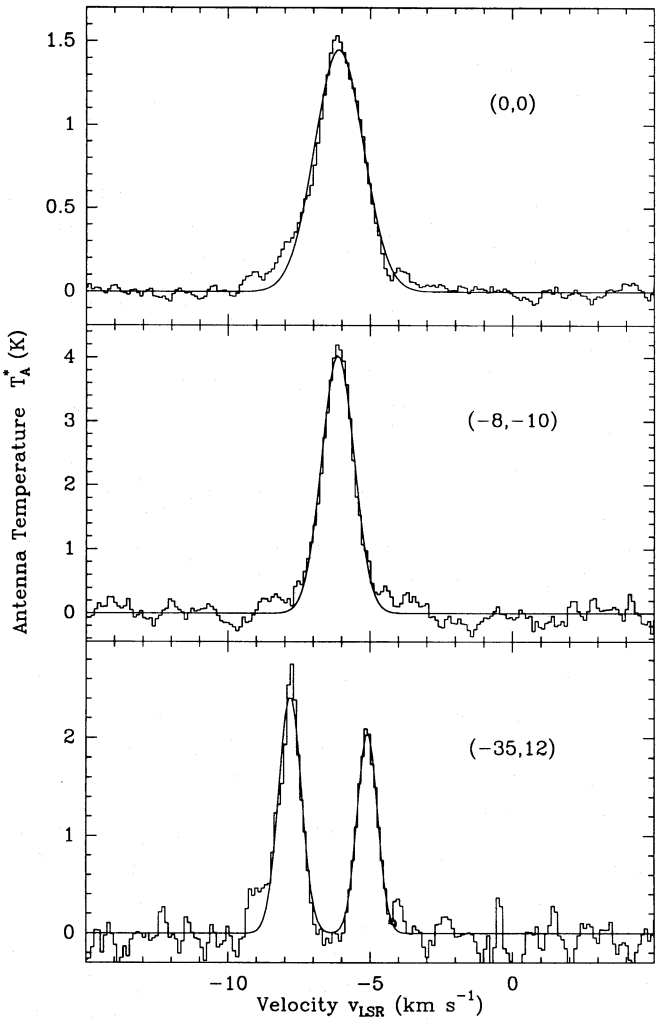

Fig. 3. The ^{12}CO spectra obtained toward HD 210121 [position (0, 0)] and at offsets (Δα, Δδ) = (−8′, −10′) and (−35′, 12′). Gaussian fits to the spectra are shown as well

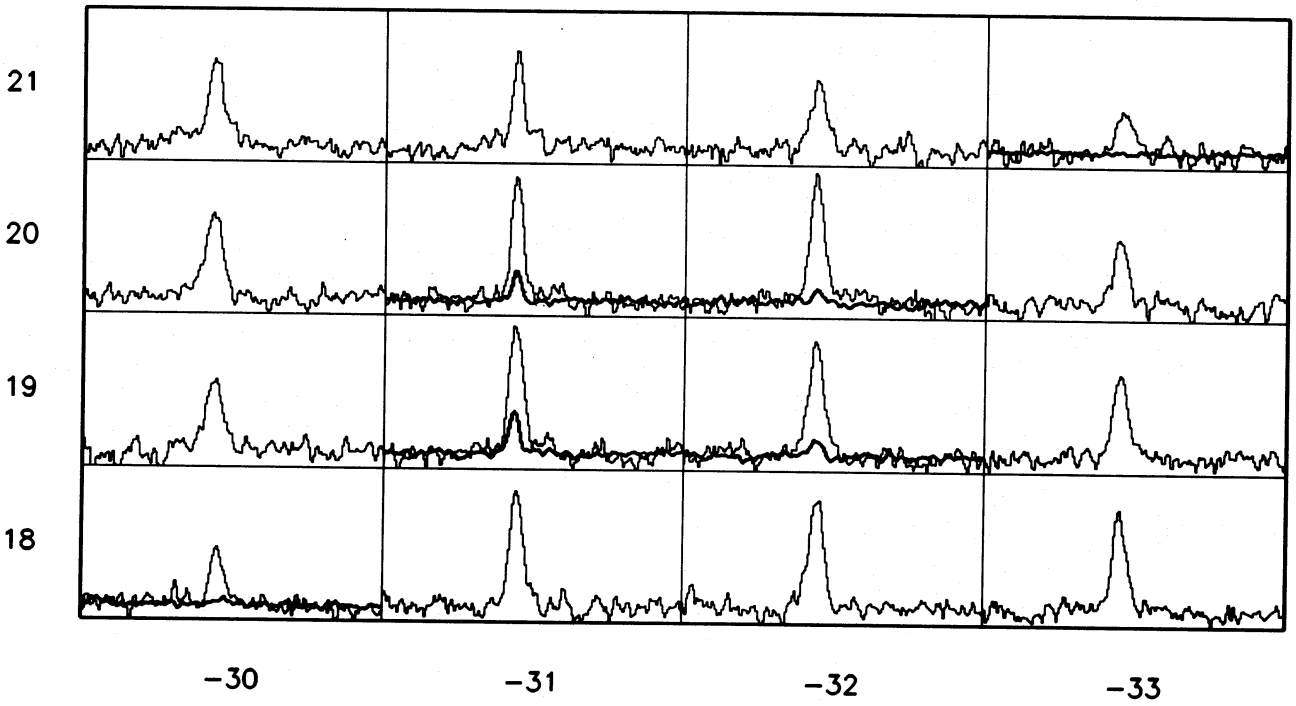

Fig. 4. Mosaic of ^{12}CO and ^{13}CO spectra obtained around (−31′, 19′) in region D. The temperature scale is $-0.5\ K < T_A^* < 4.5\ K$ for ^{12}CO and ^{13}CO. The velocity scale is $-15\ km\,s^{-1} < V_{LSR} < 5\ km\,s^{-1}$. The ^{13}CO spectra are represented by heavy lines

A few positions around location (−31, 19) were observed in ^{12}CO and ^{13}CO. The respective spectra are shown in Fig. 4, with the ^{12}CO and ^{13}CO spectra drawn at the same T_A^* scale. No double structure is seen at these positions. Clearly, the $^{12}CO/^{13}CO$ intensity ratio changes toward the edge of the clump.

Region E is a small, isolated clump around (−26, −4) south of region B. A contour plot with ^{12}CO levels ranging from 2 to 4 K in steps of 1 K is shown in Fig. 2d. ^{13}CO observations were made at offsets between (−27, −3) and (−25, −5) with a spacing of 0.5–1′. The ^{13}CO contours shown in Fig. 2d range from $T_A^*=0.5$ to 1 K in steps of 0.1 K. Both the ^{12}CO and ^{13}CO emission delineate circular regions with diameters of 3′ and 1′.5, respectively, and the emission maxima of ^{12}CO and ^{13}CO coincide.

3.2. $^{12}CO/^{13}CO$ intensity ratios

The $T_A^*(^{12}CO)/T_A^*(^{13}CO)$ intensity ratios measured at selected positions are summarized in Table 1. The ^{13}CO emission toward the star is weak and $T_A^*(^{13}CO)$ reaches only 6% of $T_A^*(^{12}CO)$. ^{13}CO is also weak around (−32, 2) where a local maximum in the ^{12}CO emission occurs. Here $T_A^*(^{12}CO)/T_A^*(^{13}CO)=9.4$. On the other hand, low ratios around 3 prevail near the two ^{12}CO maxima of regions A and B, at (−8, −10) and (−29, 3), respectively, where $T_A^*(^{12}CO)\geq 4$ K. The ratio increases to values around 10 toward the boundary of the two ^{13}CO clumps. Since the ^{12}CO emission is roughly constant across the two ^{13}CO clumps, the increase in the ratio is mainly due to a drop in the ^{13}CO antenna temperature. In general, significant increases in the ratio are observed whenever $T_A^*(^{12}CO)\leq 3$ K, but high ratios also occur near local ^{12}CO maxima in regions B, D and E, some of which lie close to the edge of the cloud. These points are illustrated in Fig. 5, where $T_A^*(^{12}CO)/T_A^*(^{13}CO)$ is plotted as a function of $T_A^*(^{12}CO)$. In classical diffuse clouds such as the ζ Oph cloud, the observed ratio is about 80 (Langer et al. 1987), whereas in the cores of Giant Molecular Clouds (GMCs), it is approximately 3–5 (Solomon et al. 1979). For large-scale emission that is averaged over both GMCs and more dilute gas, the ratio is 6.7±0.7 (Polk et al. 1988). Clearly, at many positions in the HD 210121 cloud the ratio is far from that found is GMCs, and is closer to the ratio 21±8 found by Knapp & Bowers (1988) for their tiny clouds. We will discuss the implications of the $^{12}CO/^{13}CO$ ratios in more detail in Sect. 4.2.

3.3. *Line profiles*

The CO spectra obtained at the various positions show variations in their line profiles. A few examples are given in Fig. 3. The spectra were obtained at the three positions (0, 0), (−8, −10) (in region A) and (−35, 12) (in region D). The Gaussian fits are also drawn. The ^{12}CO spectrum towards HD 210121, obtained with an integration time of 60 min, was fitted with a Gaussian of $V_{LSR} = -6.2\ km\,s^{-1}$ and $\Delta V = 2.1\ km\,s^{-1}$. The parameters for the fit to the ^{13}CO line are $V_{LSR} = -5.9\ km\,s^{-1}$ and $\Delta V = 1.7\ km\,s^{-1}$. The deviation from a single Gaussian of the ^{12}CO line profile is obvious, especially on the blue side, and may be caused by multiple, unresolved velocity components in the line of sight or wings with a width of $\approx 5\ km\,s^{-1}$. Because of the instrumental problems discussed in Sect. 2.1, care has to be taken whether the apparent wings are real. For this reason, several spectra were taken over a period of more than 2 yr, and they all systematically show an excess at blue velocities. For comparison, a 3×3 CO $J=2\rightarrow 1$ map was obtained with 10″ spacing around the star.

Although the integration time at each position was 16 min, the individual spectra are rather noisy, so that we consider only the averaged spectrum. Figure 6 (left) compares this averaged CO $J=2\rightarrow1$ profile with $1\rightarrow0$ profile at the (0, 0) position. The blue wing is clearly visible also in the $2\rightarrow1$ spectrum. Similar wings have been observed previously in high-latitude clouds by Blitz et al. (1988) and Magnani et al. (1990), and in other regions without internal energy sources or star-forming activity by Knapp & Bowers (1988) and Falgarone & Phillips (1990).

To investigate changes in the ^{12}CO emission in the neighborhood of HD 210121, a $3' \times 3'$ region around the star was mapped at 20″ (half beamwidth) spacing. The integration time at each position was 7 min, resulting in a rms of 0.09 K. These spectra are shown as a mosaic in Fig. 7, whereas the averaged profile over the whole region is compared with the $2\rightarrow1$ line in Fig. 6 (right). In addition, a five point ^{13}CO 1–0 map around the star at 20″ spacing was made, with an integration time of 70 min per point. Since $T_A^*(^{13}CO)$ is less than 0.1 K at each position with a rms of

Table 1. ^{12}CO 1–0 and ^{13}CO 1–0 observations at selected positions

$(\Delta\alpha, \Delta\delta)$ (arcmin)	$V_{LSR}(12)$ (km s^{-1})	$V_{LSR}(13)$ (km s^{-1})	$\Delta V(12)$ (km s^{-1})	$\Delta V(13)$ (km s^{-1})	$T_A^*(12)$ (K)	$\frac{T_A^*(12)}{T_A^*(13)}$	$\int T_A^*(12)\,dV$ (K km s^{-1})	$\frac{\int T_A^*(12)\,dV}{\int T_A^*(13)\,dV}$	$N(H_2)$[a] (cm^{-2})
(0, 0)	−6.2	−5.9	2.1	1.7	1.5	17.6	3.3	22.0	9.2 (20)
Region A									
(−9, −11)	−5.8	−5.9	0.9	0.8	3.7	5.5	3.7	6.6	1.1 (21)
(−8, −11)	−6.2	−5.9	1.1	0.6	3.5	3.3	4.3	6.7	1.3 (21)
(−7, −11)	−6.0	−5.9	1.3	0.6	3.5	5.5	4.6	5.6	1.4 (21)
(−6, −11)	−6.4	−6.1	1.3	0.7	4.2	4.9	5.5	8.7	1.7 (21)
(−9, −10)	−6.2	—	0.9	—	3.0	>10	2.9	—	9.0 (20)
(−8, −10)	−6.1	−5.9	1.3	0.9	4.0	3.8	5.8	5.7	1.8 (21)
(−7, −10)	−6.4	−6.1	1.0	0.7	4.5	3.7	5.0	5.1	1.5 (21)
(−6, −10)	−6.3	−6.3	1.5	1.2	3.3	5.3	5.1	6.4	1.6 (21)
(−9, −9)	−6.1	−6.4	1.4	0.7	3.2	7.8	4.8	15.5	1.5 (21)
(−8, −9)	−6.4	−6.1	1.2	0.7	4.3	6.2	5.6	11.0	1.7 (21)
(−7, −9)	−6.0	−6.0	1.1	0.8	3.4	3.0	4.0	4.0	1.2 (21)
(−6, −9)	−6.3	−5.8	0.9	0.8	2.8	5.9	2.8	6.7	8.5 (20)
(−7, −8)	−6.4	−6.2	1.2	0.7	3.2	3.9	4.0	6.9	1.2 (21)
Region B									
(−32.5, 1.8)	−7.2	−6.5	1.2	1.0	4.7	7.6	5.9	8.6	1.8 (21)
(−32.5, 2.5)	−7.1	−6.5	1.3	0.7	5.1	10.0	7.2	18.5	2.2 (21)
(−32.3, 4.5)	−7.1	−7.2	1.5	1.1	1.5	9.7	2.4	12.6	7.5 (20)
(−32.0, 2.0)	−7.2[b]	−6.6	1.1[b]	0.8	5.9[b]	9.4	6.9[b]	12.3	2.1 (21)
(−31.3, 1.3)	−6.7	−6.3	1.1	1.2	4.1	14.8	5.0	13.9	1.5 (21)
(−30.0, 1.5)	−6.8	−6.4	1.4	0.7	3.4	8.1	5.2	15.8	1.6 (21)
(−30.0, 3.0)	−6.7	−6.5	1.6	1.1	3.8	5.4	6.4	7.6	2.0 (21)
(−30.0, 4.5)	−6.8	−6.4	1.6	0.8	3.3	3.9	5.4	7.4	1.7 (21)
(−28.5, 1.5)	−6.5	−6.2	1.4	1.2	4.1	7.1	6.2	8.3	1.9 (21)
(−28.5, 3.0)	−6.7	−6.4	1.7	0.9	4.0	3.0	7.3	6.1	2.2 (21)
(−28.5, 4.5)	−6.7	−6.3	1.7	1.0	3.5	4.4	6.5	7.9	2.0 (21)
(−27.8, 1.5)	−6.4	—	1.4	—	2.9	>20	4.4	—	1.4 (21)
(−27.8, 2.3)	−6.4	−6.7	1.4	0.7	4.1	15.3	6.2	32.6	1.9 (21)
(−27.8, 3.0)	−6.7	—	1.7	—	3.5	>20	6.3	—	1.9 (21)
(−27.8, 3.8)	−6.7	−7.8	1.9	0.9	3.3	7.0	6.7	14.6	2.1 (21)
(−27.8, 4.5)	−6.8	−6.9	1.6	0.9	3.5	6.8	5.9	12.0	1.8 (21)
(−27.8, 5.3)	−7.0	−6.8	1.6	1.1	3.0	5.7	5.0	7.9	1.6 (21)
Region D									
(−35, 12)	−5.1	−5.3	0.8	0.7	2.1	21.0	1.8	25.7	5.5 (20)
	−7.8	−8.1	0.9	0.7	2.4	14.4	2.4	20.0	7.4 (20)
(−31, 19)	−6.2	−6.4	1.1	0.8	4.2	3.0	5.0	4.3	1.5 (21)
(−32, 20)	−6.2	−6.2	1.1	0.8	4.1	9.5	4.7	13.4	1.4 (21)
(−33, 21)	−5.9	—	1.4	—	1.3	>30	1.9	—	5.9 (20)
(−30, 18)	−6.0	−6.1	1.0	0.7	1.8	12.7	2.0	18.2	6.0 (20)
(−31, 20)	−6.2	−6.3	0.9	0.6	4.1	4.3	4.0	6.1	1.2 (21)
(−32, 19)	−6.2	−6.2	1.2	0.9	3.6	6.8	4.6	9.0	1.4 (21)

Table 1 (continued)

$(\Delta\alpha, \Delta\delta)$ (arcmin)	$V_{LSR}(12)$ (km s^{-1})	$V_{LSR}(13)$ (km s^{-1})	$\Delta V(12)$ (km s^{-1})	$\Delta V(13)$ (km s^{-1})	$T_A^*(12)$ (K)	$\frac{T_A^*(12)}{T_A^*(13)}$	$\int T_A^*(12)\,dV$ (K km s^{-1})	$\frac{\int T_A^*(12)\,dV}{\int T_A^*(13)\,dV}$	$N(H_2)$[a] (cm^{-2})
Region E									
(−27, −5)	−7.3	−7.3	1.2	0.8	2.8	15.6	3.5	21.9	1.1 (21)
(−26, −5)	−7.3	−7.2	1.3	1.3	3.7	8.3	4.9	8.3	1.5 (21)
(−25, −5)	−7.2	—	1.4	—	2.6	>30	3.8	—	1.2 (21)
(−27, −4)	−7.2	−7.2	1.3	1.0	4.1	8.9	5.8	11.6	1.8 (21)
(−26, −4)	−7.0	−7.1	1.4	1.0	3.5	5.0	5.2	6.8	1.6 (21)
(−25, −4)	−6.9	−6.9	1.4	0.7	2.5	4.2	3.6	8.8	1.1 (21)
(−27, −3)	−7.1	−7.0	1.2	1.7	2.9	9.9	3.8	7.0	1.2 (21)
(−26, −3)	−6.8	−6.7	1.7	1.0	2.2	6.3	4.0	11.1	1.2 (21)
(−25, −3)	−6.7	—	1.9	—	1.8	>37	3.7	—	1.1 (21)

Note: 12 stands for ^{12}CO, 13 for ^{13}CO

[a] As determined using the standard conversion factor given by Bloemen et al. (1986)

[b] ^{12}CO measured position (−31.75, 1.75)

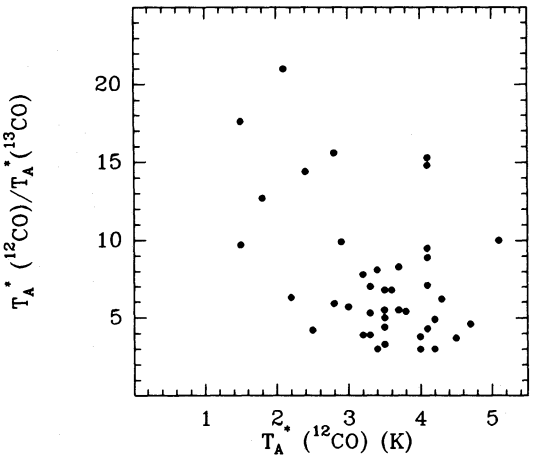

Fig. 5. The ratio of intensities, $T_A^*(^{12}CO)/T_A^*(^{13}CO)$, as a function of $T_A^*(^{12}CO)$

0.03 K, the S/N is not high, so that the spectra are not presented. No significant changes in ^{13}CO line strength were found over this area. All spectra around HD 210121 were taken in May 1991, when the rejection of the PLL sidelobes was much better than during previous runs, and reproduceable spectra were obtained. The maps of peak and integrated antenna temperatures are presented in Fig. 8 (top), together with velocity channel maps at 0.25 km s^{-1} interval (bottom). Apart from an overall gradient in intensity from NW to SE, the integrated maps reveal little structure. The channel maps show a lack of discrete features around the central velocity $V_{LSR} \approx -6.5$ km s^{-1}, but at other velocities (e.g. $V_{LSR} = -6$ to -5.5 km s^{-1}) fairly isolated "cells" may be seen at the 2–3σ level. The "cell" at $V_{LSR} = -6$ km s^{-1} has a diameter of about 60″, i.e. slightly larger than the beam size of 45″. Any apparent feature in these maps with a half-power size smaller than the primary beam size is probably artificial. This small-scale structure will be analysed further in Sect. 4.2.2.

3.4. Velocity structure

The velocity structure of the HD 210121 cloud is summarized in Table 2. The analysis considers separately the ^{12}CO and ^{13}CO data for the 5 individual regions marked in Fig. 1b. The terms D_1 and D_2 refer to the line components at -5 km s^{-1} and -8 km s^{-1}, respectively, in region D. Columns 2 and 3 list the mean full width at half maximum $\overline{\Delta V}$ and the mean radial velocity $\overline{V_{LSR}}$ of the CO profiles, with individual data weighted by $\int T_A^* dV$. The respective standard deviations are given in parenthesis. Column 4 lists the point to point velocity dispersion σ_{int} as defined through

$$\sigma_{int} = \frac{N}{N-1} \frac{\Sigma \int T_A^* dV (V_i - \bar{V})^2}{\Sigma \int T_A^* dV}.$$

The summation is carried out over all N individual positions with $T_A^* > 1$ K. The entries listed in column 5 refer to the total one dimensional velocity dispersion σ_z which is calculated according to $\sigma_z = [(\overline{\Delta V}/2.35)^2 + \sigma_{int}^2]^{1/2}$. The values listed in Table 2 indicate that the bulk ^{12}CO emission of the individual regions A–E occurs at almost constant velocity. For example, in the region around the direction to HD 210121, the velocity changes by no more than 0.4 km s^{-1} over 14′.2, which corresponds to $|dV/dR| \approx$ 0.65 km s^{-1} pc^{-1}. The internal velocity dispersion σ_{int} of each of the 5 regions A–E is typically a factor of 3 smaller than the mean FWHM calculated from the individual spectra. The slightly higher mean velocity dispersion of region B may be caused by the contribution of a second, unresolved emission component at $V_{LSR} \approx -8$ km s^{-1}. The relevant spectra show a hint of such a component, but since they have rather low signal to noise ratios no attempt was made to fit two Gaussians to the spectra. The complete sample of ^{12}CO profiles is characterized by a total line width of 1.9 km s^{-1}. This implies a mean line-of-sight velocity gradient of $|dV/dR| \approx 0.7$ km s^{-1} pc^{-1}, if the thickness of the cloud is assumed to be comparable to its projected diameter, 2.6 pc. No significant change in FWHM occurs between spectra with low T_A^* and those with high T_A^*. The ^{13}CO spectra have significantly lower values of ΔV, but the ^{13}CO emission occurs at

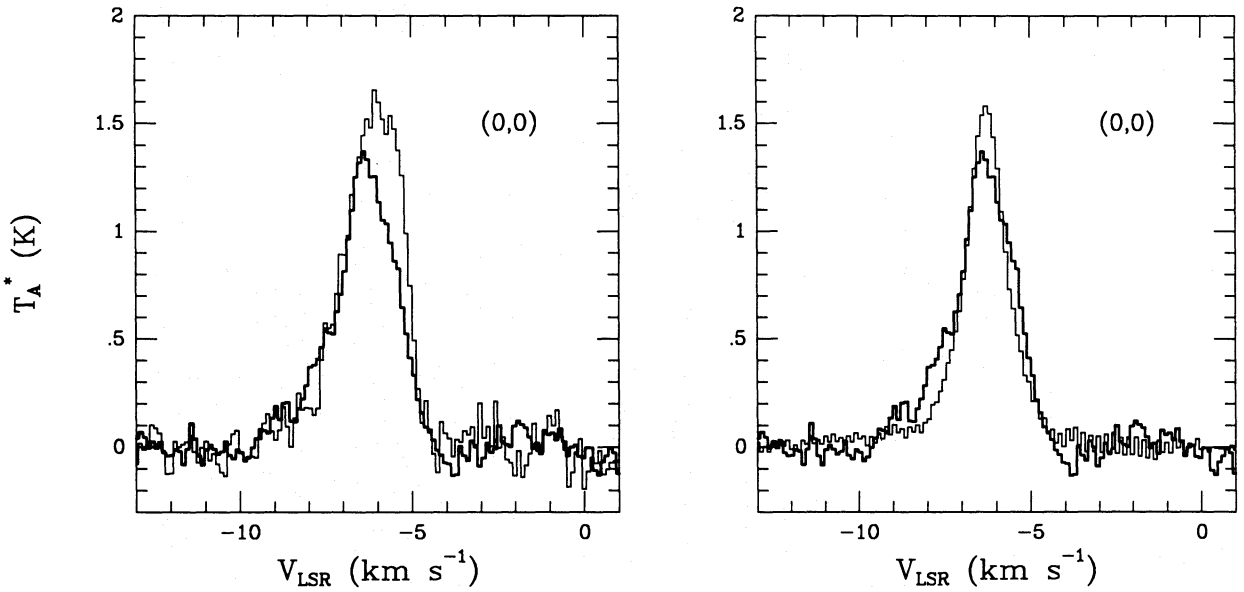

Fig. 6. *Left*: Comparison of ^{12}CO $J=2\rightarrow1$ (heavy line) and $1\rightarrow0$ (light line) profiles toward the star. The $2\rightarrow1$ profile was obtained by averaging 9 spectra with integration times of 16 min each taken at 10″ steps around the star. Note that the calibration of the $2\rightarrow1$ line is highly uncertain. *Right*: Comparison of the same ^{12}CO $2\rightarrow1$ profile with the $1\rightarrow0$ profile obtained by averaging all spectra presented in Figure 7 in the $3'\times3'$ region around the star

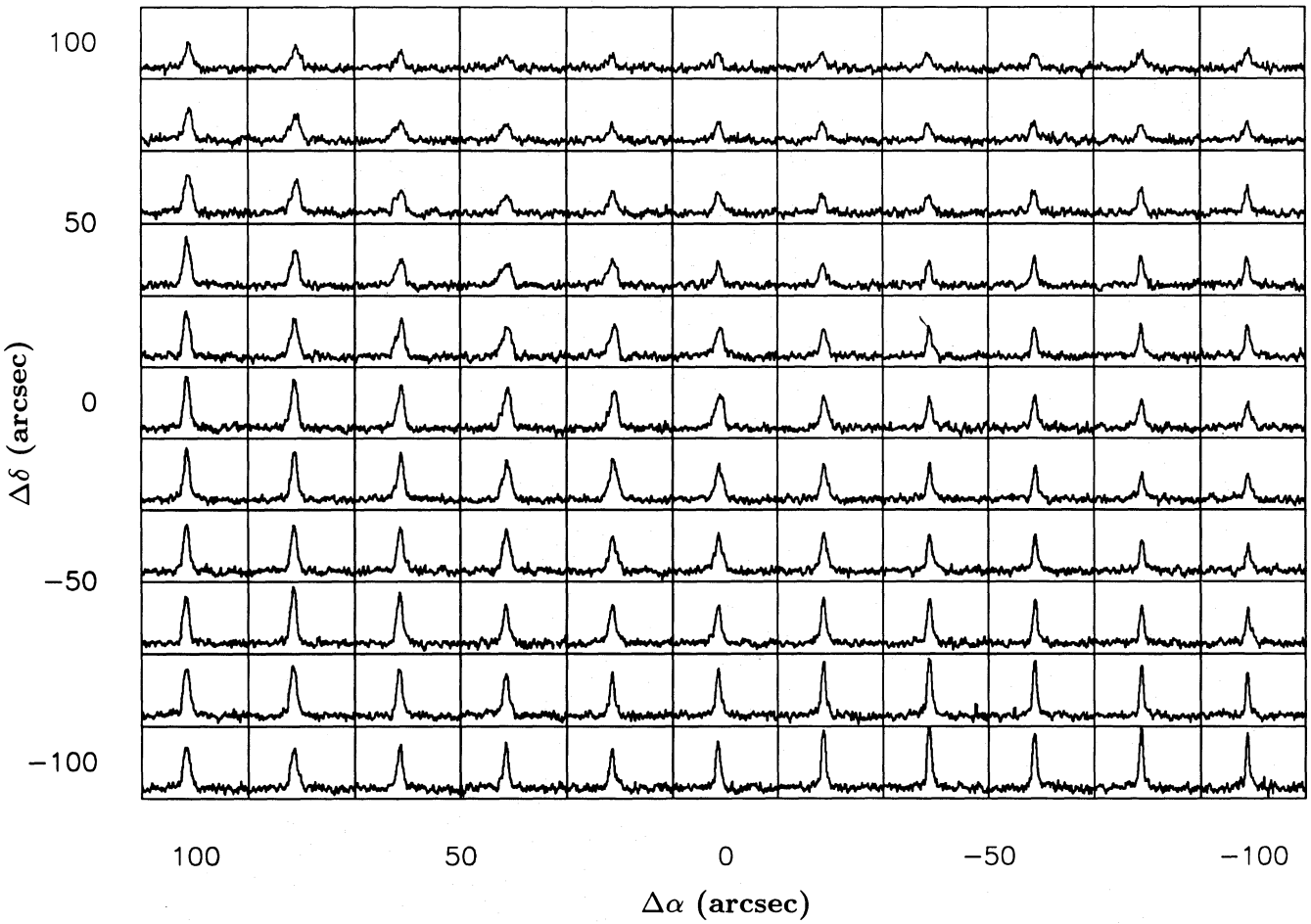

Fig. 7. Mosaic of ^{12}CO $J=1\rightarrow0$ spectra around HD 210121. The offset between individual positions is 20″. The velocity scale for each of the spectra is $-15\ \mathrm{km\,s^{-1}} < V_{LSR} < 5\ \mathrm{km\,s^{-1}}$. The temperature scale is $-0.5\ \mathrm{K} < T_A^* < 3\ \mathrm{K}$

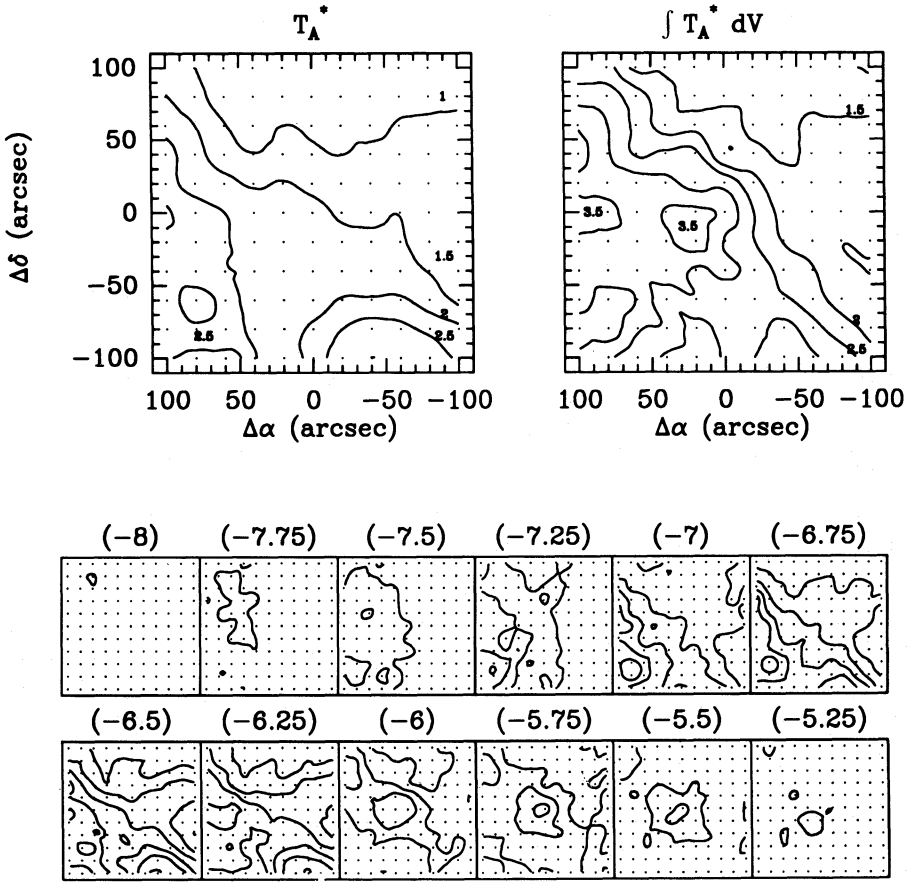

Fig. 8. Map of ^{12}CO peak antenna temperature T_A^* (left) and integrated antenna temperature $\int T_A^* dV$ (right) of the region around HD 210121. Contour levels are indicated in the figure. The mosaic in the lower part of the figure shows individual channel maps, with the velocity indicated above each map. The lowest contour in these maps is 0.1 K, except for $V_{LSR} = -6.75$, -6.5 and -6.25 km s^{-1}, where the lowest contour is 0.2 K. The increment in the contour levels is 0.1 K

Table 2. The velocity structure of the cloud

Region	$\overline{\Delta V}^a$ (km s^{-1})	$\overline{V_{LSR}}^a$ (km s^{-1})	σ_{int} (km s^{-1})	σ_z (km s^{-1})
^{12}CO 1–0 data				
Total	1.4 (0.4)	−6.3 (0.7)	0.5	0.8
A . . .	1.3 (0.3)	−6.2 (0.3)	0.3	0.6
B . . .	1.6 (0.4)	−6.6 (1.1)	0.5	0.8
C . . .	1.4 (0.4)	−6.6 (0.4)	0.4	0.7
D_1 . . .	1.4 (0.7)	−6.1 (0.7)	0.6	0.8
D_2 . . .	1.3 (0.3)	−7.5 (0.5)	0.5	0.7
E . . .	1.6 (0.4)	−6.8 (0.4)	0.4	0.8
^{13}CO 1–0 data				
Total	0.9 (0.3)	−6.3 (0.8)	0.5	0.6
A . . .	0.9 (0.3)	−6.0 (0.2)	0.2	0.4
B . . .	0.9 (0.3)	−6.6 (1.3)	0.7	0.8
E . . .	1.0 (0.2)	−7.1 (0.1)	0.1	0.4

[a] weighted with $\int T_A^* dV$; standard deviation in parenthesis

the same radial velocities as does the ^{12}CO emission within the errors. The internal velocity dispersion of regions A and B, as derived from the ^{13}CO spectra, is similar to that obtained from the ^{12}CO data.

3.5. H_2 column densities and masses

The H_2 column densities and masses of high-latitude clouds have so far been determined mostly on the basis of the ^{12}CO emission data. As shown by de Vries & van Dishoeck (1988), the availability of absorption line observations toward HD 210121 allows independent determinations of the H_2 column density for at least one position in the cloud, against which the CO/H_2 conversion factors can be calibrated. The CH observations suggest $N(H_2) \approx 10^{21}$ cm^{-2}, based on the empirical relationship between CH and H_2 found by Danks et al. (1984) in diffuse clouds and by Mattila (1986) in dark clouds. The visual extinction $A_V \approx 1$ mag implies a total hydrogen column density of $N_H = N(H) + 2N(H_2) = 1.6\ 10^{21}$ cm^{-2} if a standard gas to extinction ratio applies. Since the atomic hydrogen column density is estimated to be $N(H) \approx (1\text{–}5)\ 10^{20}$ cm^{-2} from the survey data of Heiles & Habing (1974; see also de Vries & van Dishoeck 1988; Stark et al. 1992 in preparation), the H_2 column density based on the extinction is about (6–8) 10^{20} cm^{-2}. Thus, on the basis of the optical data, the H_2 column density toward HD 210121 is estimated to be $N(H_2) \approx (8 \pm 2)\ 10^{20}$ cm^{-2}. A similar value can be derived from the IRAS 100 μm flux. This H_2 column density agrees well with that obtained from the ^{12}CO integrated intensity $\int T_A^* dV = 3.3$ K km s^{-1} or $\int T_R dV = 3.6$ K km s^{-1} if the standard conversion factor $N(H_2)/I_{CO} \approx 2.8\ 10^{20}$ cm^{-2} K^{-1} km^{-1} s (Bloemen et al. 1986; Magnani et al. 1988) is used. On the other hand, the lower conversion factors derived by de Vries et al. (1987) and Herbstmeier et al. (1989) would imply molecular column densities

in the HD 210121 cloud that are significantly lower. The standard value will therefore be applied here.

As demonstrated previously for the translucent cloud toward HD 169454 (Jannuzi et al. 1988), the standard analysis of ^{13}CO data (cf. Dickman 1978) yields H_2 column densities that are much too small. In the case of HD 210121, the measured $\int T_A^* dV = 0.15$ K km s^{-1} for ^{13}CO gives $N(H_2) = 7.5\ 10^{19}$ cm^{-2}, an order of magnitude below the estimate from the optical data. The standard analysis fails mostly because the true abundance ratio $N(^{13}CO)/N(H_2)$ is substantially smaller than the "standard" value of $2\ 10^{-6}$ found in dark clouds. In the translucent clouds not all carbon has been converted into CO, and the $^{12}CO/^{13}CO$ abundance ratio may suffer depth-dependent fractionation effects (van Dishoeck & Black 1988). In general, the H_2 column densities calculated from ^{12}CO are at least a factor of 5 higher than computed from the ^{13}CO data using the standard method of Dickman. The discrepancies tend to be smaller if $T_A^*(^{12}CO)$ is high, but exceptions occur there as well. An example is the region at offsets around (−32, 2) where $T_A^*(^{12}CO) \approx 5$ K, but $N(H_2)$ derived from the ^{12}CO and ^{13}CO measurements in the standard way differ by a factor of 10.

The maximum values of $\int T_A^* dV \approx 7.3$ K km s^{-1} observed around (−30, 3) in region B suggest that the maximum H_2 column densities in the HD 210121 cloud are only a factor of two higher than toward the star, and that the maximum visual extinction is about 3 mag, provided that $N(H_2)$ really is proportional to $\int T_A^* dV$ within such a cloud. This point will be discussed in a future paper in connection with IRAS 100 μm maps and extinction measurements toward background stars in this region (Stark et al. 1992 in preparation).

The H_2 column densities obtained with the Bloemen et al. conversion factor were used to compute hydrogen masses of the various regions by assuming spherical symmetry. For each region, the average integrated CO intensity listed in column 5 of Table 3 was adopted in this analysis. The area A of a clump is defined by a boundary contour which corresponds to $1/e$ of the maximum CO intensity in the respective region. For the total cloud, a boundary value of 1 K km s^{-1} was chosen. The resulting molecular masses M_H are listed in column 7 of Table 3. In order to obtain the total masses M including He, M_H has been multiplied by a factor 1.4. The total mass of the cloud is $M_H \approx 334 M_\odot$, which is a factor of 2.2 times higher than the sum of the masses of the individual regions because of the additional gas that contributes low-level emission outside the five regions A–E. The total CO intensity integrated over the whole area of the HD 210121 cloud is $\int T_A^* dV d\alpha d\delta \approx 3700$ K km s^{-1} (arcmin)^2.

These masses can be compared with those derived from the virial theorem. The three-dimensional velocity dispersion σ_{3d} listed in column 2 of Table 3 has been obtained from $\sqrt{3}\sigma_z$, where σ_z has been listed in Table 2. It ranges from 0.8 km s^{-1} $< \sigma_{3d} < 1.5$ km s^{-1}. If the kinetic temperature is $T \approx 15$ K (see Sect. 3.6.1), σ_{3d} is primarily non-thermal or macroscopic. If we assume virial equilibrium between the gravitational potential and the kinetic energy and neglect other terms arising, for example, from magnetic fields or external pressures, the masses of the individual regions can be calculated from the line width. In particular, for a uniform sphere the virial theorem reduces to $M_{virial} = 5R\sigma_{3d}^2/3G$ where $R = \sqrt{A/\pi}$. The virial masses so obtained are listed in column 6 of Table 3 and range from 70–240 $M_\odot$ for regions A–E and $\approx 670 M_\odot$ for the total cloud. In general, the masses of individual clumps derived from the H_2 column densities are significantly smaller than the virial masses, $M/M_{virial} \approx 0.1$–0.5, suggesting that gravity is not important maintaining their structure. On the other hand, the two determinations differ by only 30% for the cloud as a whole, which may imply that the overall structure is gravitationally bound.

3.6. *Inferred physical parameters*

Ever since the detection of the high-latitude clouds, their physical conditions such as temperature and density have been the subject of considerable speculation. For the HD 210121 cloud, we have several independent probes available.

3.6.1. C_2 excitation

The absorption lines of C_2 toward HD 210121 provide in principle an excellent diagnostic tool. The theory of the excitation of C_2

Table 3. Masses of individual regions

Region	σ_{3d} (km s^{-1})	Boundary[a] (K km s^{-1})	A[b] (arcmin)^2	$\langle \int T_A^* dV \rangle$ (K km s^{-1})	M_{virial}^c $(D/150)\,M_\odot$	M_H^d $(D/150)^2\,M_\odot$	M/M_{virial}^e
Total	1.3	1.0	1750	2.07	670	334	0.7
A . . .	1.1	2.5	155	3.31	143	47	0.5
B . . .	1.5	3.0	122	4.25	236	48	0.3
C . . .	1.2	2.0	132	2.67	157	33	0.3
D_1 . . .	1.5	2.0	42	3.16	138	12	0.1
D_2 . . .	1.3	1.0	20	1.93	72	4	0.1
E . . .	1.4	2.5	23	3.66	89	8	0.1

[a] Boundary contour $\int T_A^* dV$ for determination area A
[b] Area within boundary
[c] $M_{virial} = 5R\sigma_{3d}^2/3G = 16.8\ \sigma_{3d}^2\ (D/150)\ \sqrt{A/\pi}$
[d] $M_H = 0.084\ A\ (D/150)^2\ \langle \int T_a^* dV \rangle \eta_{Moon}^{-1}$
[e] $M = 1.4\ M_H$
D: Distance in pc; A: Area in (arcmin)^2; σ_{3d}: three-dimensional velocity dispersion in km s^{-1}

was developed by van Dishoeck & Black (1982), and has subsequently been applied successfully to diffuse and translucent clouds (van Dishoeck & de Zeeuw 1984; Gredel & Münch 1986; van Dishoeck & Black 1989). The C_2 populations result from the competition between a radiative pumping process at far-red wavelengths ($\lambda \approx 1\,\mu m$), and collisional excitation and de-excitation processes.

Unfortunately, the signal to noise in the C_2 spectrum toward HD 210121 is quite low, in spite of 5 h of integration, so that the analysis is quite uncertain. The spectrum is presented in Fig. 9, while Table 4 summarizes the measured equivalent widths for the lines and the derived column densities. For details concerning the adopted oscillator strengths and wavelengths, see van Dishoeck & Black (1989). In Fig. 10, the derived population ratios are plotted as functions of excitation temperature of the level. For comparison, the theoretical excitation curves for $T=15$ K and n ranging from 50 to 300 cm^{-3} are shown, assuming that the C_2–H_2 collisional cross section $\sigma_0 \approx 2\ 10^{-16}\,cm^2$ and that the radiation field at red wavelengths is not enhanced over its standard value, $I_R \approx 1$. The populations of the lowest levels, $J=0$ and 2, are sensitive primarily to temperature and suggest that the high-latitude cloud is quite cold, $T \lesssim 20$ K. The populations of the higher levels constrain the density. The very low column density in the $J=6$ level appears to indicate a rather high density $n \geq 300\ cm^{-3}$ toward HD 210121. On the other hand, the fact that the Q(8) line is readily observable suggests a lower density, $n \approx 250\ cm^{-3}$. Note that the Q(8) feature at 8773 Å is actually a blend of the Q(8) and P(4) lines. Based on the strength of the Q(4) line, we estimate the P(4) line to contribute about 2 mÅ to the blend. This contribution has already been taken into account in the $J=8$ column density listed in Table 4.

In summary, the C_2 excitation indicates a rather low temperature, $T \lesssim 20$ K along the line of sight toward HD 210121 and an uncertain density. If the Q(8) line is indeed as strong as suggested, the best estimate of the density is quite low, $n \approx 250\ cm^{-3}$, corresponding to $n_H = n + n(H_2) \approx 500\ cm^{-3}$. On the other hand, the virtual absence of the Q(6) line suggests higher densities. Higher S/N ratios in the C_2 spectra are needed to settle this issue.

Table 4. Interstellar C_2 observations toward HD 210121

Line	W_λ (mÅ)	N_J (cm^{-2})
R (0)	3.6±0.8	(5.3±1.0) (12)
Q (2)	5.6±1.5	(1.6±0.4) (13)
R (2)	3.9±0.5	(1.4±0.3) (13)
P (4)[a]	≈2	—
Q (4)	5.6±1.5	(1.6±0.4) (13)
R (4)	3.5±1.1	(1.5±0.5) (13)
Q (6)	≤3	≤0.9 (13)
Q (8)[a]	2±1	(6±3) (12)
Total[b]		(6.5±1.5) (13)

[a] P (4)+Q(8): 4±2 mÅ; P(4) estimated from Q(4)
[b] Total C_2 column density, including contribution from unobserved levels

3.6.2. CN excitation

The CN excitation can also provide limits on the density, although in a more indirect way, as illustrated in detail by Black & van Dishoeck (1991a). In diffuse and translucent clouds, the excitation of a molecule with a large dipole moment like CN above the cosmic background radiation is caused primarily by collisions with electrons. The absorption spectrum toward HD 210121 in the region around 3875 Å is presented in Fig. 11. The CN R(0), R(1) and P(1) blends are clearly identified, in addition to some weak lines of CH in the $B^2\Sigma^- - X^2\Pi$ (0, 0) band. The measured equivalent widths are summarized in Table 5, together with upper limits on the R(2) and P(2) lines. The analysis adopts a Doppler parameter $b = \Delta V/1.665 = 1.0\ km\ s^{-1}$ and uses the same molecular data and method as described in Black & van

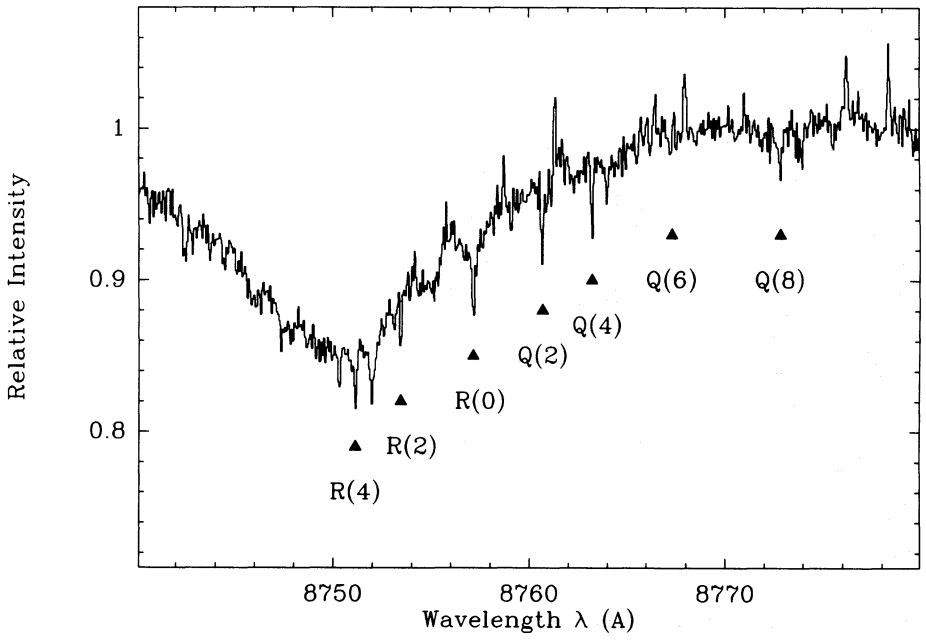

Fig. 9. Spectrum toward HD 210121 in the region of the C_2 (2, 0) Phillips band. The various interstellar C_2 lines are indicated

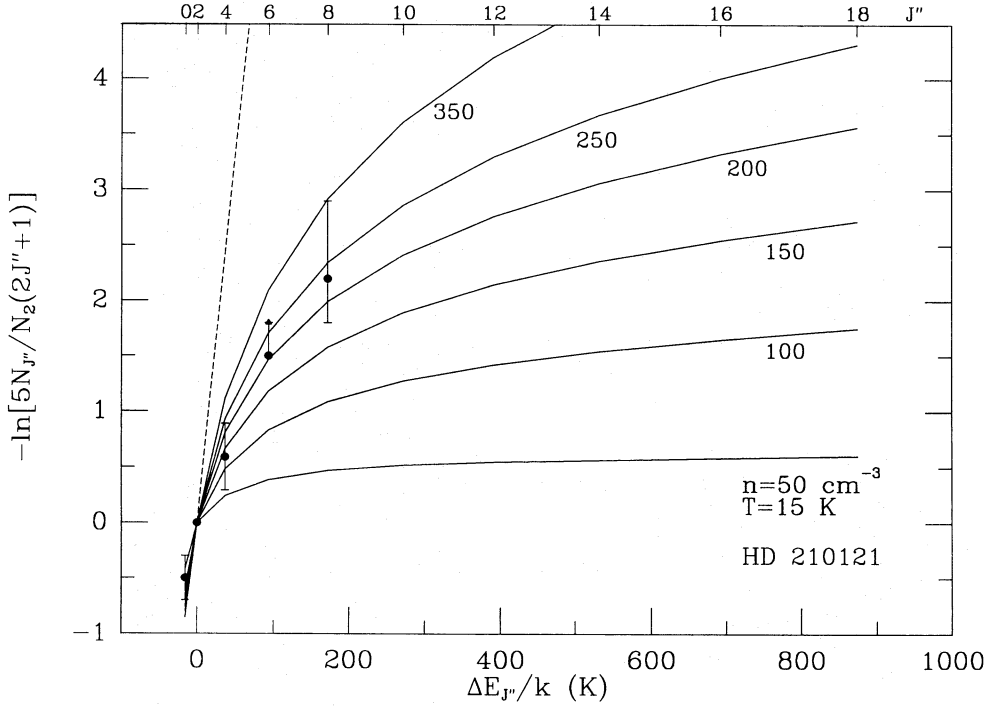

Fig. 10. Comparison between the observed rotational population distribution of C_2 toward HD 210121 (filled dots) and the theoretical distributions (full lines) at a kinetic temperature $T=15$ K and densities ranging from $n=n(H)+n(H_2)=50$ to 350 cm^{-3}. The calculations assume $I_R=1$ and $\sigma_0=2\,10^{-16}$ cm^2. The dashed line is the thermal distribution at $T=15$ K

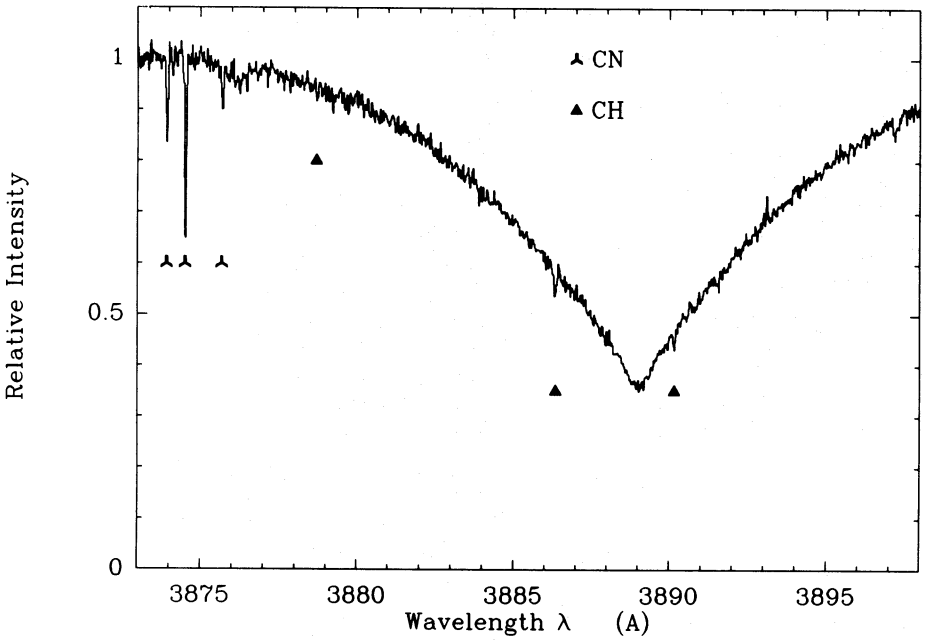

Fig. 11. Spectrum toward HD 210121 showing interstellar CN and CH absorption lines

Dishoeck (1988; 1991a) and Gredel et al. (1991). The ratio of column densities in $N=0$ and 1 gives $T_{ex}=2.8\pm0.2$ K. Comparison with the very accurately determined cosmic background temperature $T_{bg}=2.735\pm0.06$ K by COBE (Mather et al. 1990) indicates an excitation of at most 25 mK above the background radiation. This limit is consistent with searches for the CN $N=1\rightarrow0$ millimetre lines at 113.5 GHz toward the star, where no emission is found at the level of $T_A^*\lesssim27$ mK. The chemical models discussed in Sect. 4.2 below can be used to estimate the electron fraction $n(e)/n$ where $n=n(H)+n(H_2)$ is the density of neutral collision partners. The values of $n/n(e)$ are 10^4, $1.5\,10^4$, and $2.9\,10^4$, for models 1, 2, and 3, respectively. Detailed statistical equilibrium calculations have been performed for CN (see Black & van Dishoeck 1991a for details). The CN column density is fixed at the value determined from the absorption lines toward HD 210121, $N(CN)=1.2\,10^{13}$ cm^{-2}. The observed $N=0/N=1$ rotational excitation temperature, $T_{ex}=2.8$ K, requires $n(e)=0.05$–0.10 cm^{-3} and $n=1000$–1500 cm^{-3}, for the range of electron fractions suggested by the chemical models. The uncertainty in the measured excitation allows $T_{ex}\leq3.0$ K, and a correspond-

ing limit on derived density, $n \lesssim 3800\ \mathrm{cm}^{-3}$. The limit on the $N=1\rightarrow0\ J=3/2\rightarrow1/2\ F=5/2\rightarrow3/2$ hyperfine-structure component at 113.491 GHz provides an independent estimate of the density: $n \lesssim 600\ \mathrm{cm}^{-3}$ at $n/n(e)=10^4$, or $n \lesssim 850\ \mathrm{cm}^{-3}$ at $n/n(e)=2.9\,10^4$. In the models, $N(\mathrm{H})/N(\mathrm{H_2})<0.1$, so that $n \approx n(\mathrm{H_2})$.

Thus, the observations of CN suggest $n \approx n(\mathrm{H_2}) \approx$ 600–1500 cm^{-3} toward HD 210121, and provide a firm upper limit of $n \lesssim 3800\ \mathrm{cm}^{-3}$. The absence of significant CN millimetre emission toward the peak positions in clumps A and B indicates that the densities and CN column densities at those off positions cannot be enhanced compared with the line of sight toward the star.

3.6.3. CO excitation

Yet another method to derive densities in translucent clouds is to compare the strength of the CO $J=3\rightarrow2$ emission line at 345 GHz with that of the $J=2\rightarrow1$ or $1\rightarrow0$ line. This method has recently been explored in detail by van Dishoeck et al. (1991) and has yielded densities of the order of $n=1000$–$5000\ \mathrm{cm}^{-3}$ toward HD 210121. Similar densities were found toward the peak CO positions in region A (−8, −10) and B (−32.5, 0). Only along a small north–south strip across region B was some evidence found for variations in density by factors of a few from the edge of the region to the center. In general, the densities derived from the ^{12}CO $J=1\rightarrow0/3\rightarrow2$ ratio were found to be higher than those inferred from the optical C_2 data. The reasons for this discrepancy are not yet fully understood, but several possible explanations have been discussed by van Dishoeck et al. (1991). It should also be recalled that it has only recently been realized that the SEST $J=1\rightarrow0$ antenna temperatures may be systematically too low, and that this may have resulted in overestimates of the density. We therefore use the above densities derived from the ^{12}CO excitation as upper limits to the true density. The ^{12}CO $J=3\rightarrow2/^{13}$CO $J=1\rightarrow0$ ratio indicates densities around $n=1000$–$2000\ \mathrm{cm}^{-3}$, closer to those found from the C_2 data.

In summary, the C_2 excitation analysis results in a rather low temperature, $T \lesssim 20$ K in the cloud. The C_2 and CN data favor H_2 densities of a few hundred to $1000\ \mathrm{cm}^{-3}$, whereas the CO excitation indicates densities that are somewhat higher, up to $5000\ \mathrm{cm}^{-3}$, but with no significant variation from place to place.

4. Chemical properties of the cloud

4.1. Observed molecular abundances

Although quite a number of molecules have been discovered in high-latitude clouds, few have been observed at the same position in a cloud. Moreover, those positions are often poorly characterized in terms of physical conditions and total H_2 column density, making the derivation of abundances with respect to H_2 very uncertain. As a result, a number of claims have appeared in the literature which state that the molecular abundances in high-latitude clouds are "abnormal", either abnormally high (Magnani et al. 1988) or abnormally low (Turner et al. 1989). We demonstrate here that the molecular abundances in high-latitude clouds are entirely consistent with those found in diffuse and translucent clouds, at least for the well-characterized line of sight toward HD 210121.

The column densities of CH, C_2, CN and CH^+ inferred from the optical data are well determined and are included in Table 6.

Table 5. Interstellar CN and CH observations toward HD 210121

Line	λ_{rest} (Å)	W_λ (mÅ)	N_J (cm^{-2})
CN $R_1(0)$	3874.607	(23.4 ± 2.0)	(8.5 ± 1.0) (12)
CN $R_1(1)$	3873.999	(10.0 ± 0.9)	(3.9 ± 0.5) (12)
CN $P_1(1)$	3875.764	(4.9 ± 0.9)	(3.5 ± 0.5) (12)
CN $R_1(2)$	3873.370	≤2	≤7 (11)
CN $P_1(2)$	3876.312	≤2	≤1 (12)
CN $R_1(0)$	7906.601	≤3	≤1.4 (13)
CH $^{\mathrm{P}}Q_{12}(1/2)$	3890.217	(3.5 ± 1.4)	(1.2 ± 0.5) (13)[a]
CH $R_2(1/2)$	3878.774	≤3	≤2 (13)[a]
CH $Q_2(1/2)$	3886.407	(6.7 ± 1.5)	(3.1 ± 0.7) (13)[b]
CH $R_f(1/2)$	4300.313	22 ± 4	(3.4 ± 0.4) (13)[c]

[a] Column density of one Λ-sublevel only
[b] Blend: column density of both sublevels
[c] Column density of both sublevels for $b=1.0\ \mathrm{km\,s}^{-1}$ (cf. de Vries & van Dishoeck 1988)

Table 7 summarizes the searches for molecules at millimetre wavelengths. Derivation of column densities from millimetre data is more uncertain, however. Let us first take the important case of ^{12}CO. The large ratio $T_A^*(^{12}\mathrm{CO})/T_A^*(^{13}\mathrm{CO}) \approx 20$ toward the star indicates that the ^{12}CO optical depth must be small. For a ^{12}CO/^{13}CO abundance ratio of 60, this would imply $\tau \approx 3$. The optical depth could be much lower, however, since ^{13}CO may be significantly fractionated in this cold ($T \approx 15$ K) cloud of low total column density. The detailed models of van Dishoeck & Black (1988) suggest enhancement factors of three or more under these conditions, which would lead to $\tau \lesssim 1$. The resulting column density for a homogeneous cloud can be estimated from statistical equilibrium calculations, which have been performed for a range of temperatures and densities in the manner described by Jannuzi et al. (1988) and van Dishoeck et al. (1991). The observed line strength toward the star, $T_R^*=1.7$ K, can be reproduced for $T=15$–30 K and $n=200$–$5000\ \mathrm{cm}^{-3}$ with $N(\mathrm{CO})=2\,10^{15}$–$1\,10^{16}\ \mathrm{cm}^{-2}$, assuming that the emission completely fills the beam. The low end of this column density range refers to the high density, high temperature limit, while the higher column densities are found for the low temperature, low density regime. If we restrict the range of physical conditions to those derived in Sect. 3.6, we find $N(^{12}\mathrm{CO})=(7\pm3)\,10^{15}\ \mathrm{cm}^{-2}$. These calculations employ an escape probability method for the radiative transfer with the observed line width $\Delta V=2.1\ \mathrm{km\,s}^{-1}$, but identical results are obtained if a more detailed large velocity gradient or microturbulent method is applied to a homogeneous emitting region. We also note that if this same analysis is applied to the line of sight toward ζ Oph, which has a comparable CO 1–0 antenna temperature, the resulting ^{12}CO column density of a few times $10^{15}\ \mathrm{cm}^{-2}$ agrees well with that derived from UV absorption lines toward the star. For a CO column density of $7\,10^{15}\ \mathrm{cm}^{-2}$, the CO abundance with respect to H_2 is about 10^{-5}. This fraction is small compared with the solar abundance of carbon of $4.7\,10^{-4}$, and with the total amount of gas-phase carbon in all forms, which is about 10^{-4} for any reasonable grain model. This implies that most of the gas-phase carbon is still in atomic form in this cloud, a conclusion which is not changed if the possibly inhomogeneous structure of the cloud is taken into account (see Sect. 4.2.2).

Table 6. Observed and computed column densities[a] for the cloud toward HD 210121

Species/ parameter	Model[b]							HD 210121	ζ Oph	HD 169454
	1	1[c]	2	3	3[c]	4	5			
n_H (cm^{-3})	500	500	1500	5000	5000	1500	1500			
T(K)	20	20	15	15	15	15	15			
I_{UV}	0.5	0.5	0.5	0.5	0.5	1.0	0.5			
δ_C	0.1	0.1	0.1	0.1	0.04	0.1	0.1			
δ_S	0.2	0.2	0.05	0.05	0.02	0.05	0.05			
H_2	8.0 (20)	8.0 (20)	8.0 (20)	8.0 (20)	8.0 (20)	8.0 (20)	1.0 (21)	(8±2) (20)	(4.2±0.3) (20)	(1.8±0.4) (21)
H	6.8 (19)	6.7 (19)	2.9 (19)	1.5 (19)	8.4 (18)	5.0 (19)	5.0 (19)	(1–5) (20)	(5.2±0.2) (20)	≥2 (20)
C^+	6.8 (16)	5.5 (16)	5.8 (16)	3.7 (16)	9.9 (15)	6.9 (16)	6.2 (16)	—	(1±0.5) (17)	—
C	4.2 (15)	4.5 (15)	7.8 (15)	1.2 (16)	3.3 (15)	5.1 (15)	9.5 (15)	—	(3.2±0.6) (15)	—
CO	5.0 (15)	1.8 (16)	9.3 (15)	2.4 (16)	1.7 (16)	2.1 (15)	2.4 (16)	(7±3) (15)	(2.0±0.3) (15)	(2±1) (16)
^{13}CO	2.0 (14)	5.4 (14)	5.0 (14)	9.1 (14)	4.2 (14)	1.4 (14)	8.5 (14)	(2±1) (14)	(3.6±1.0) (13)	(1.1±0.4) (15)
$C^{18}O$	3.8 (12)	1.1 (13)	6.0 (12)	9.2 (12)	9.5 (12)	1.9 (12)	1.2 (13)	≤7(13)	—	—
CH	4.0 (13)	3.5 (13)	7.7 (13)	9.9 (13)	3.3 (13)	5.7 (13)	8.9 (13)	(3.5±0.5) (13)	(2.5±0.3) (13)	(5.8±0.8) (13)
CH^+	4.1 (10)	3.9 (10)	4.4 (10)	1.5 (10)	5.6 (9)	1.1 (11)	1.0 (11)	(6±2) (12)	(2.9±0.3) (13)	(3.0±1.0) (13)
C_2	5.1 (13)	4.8 (13)	2.1 (14)	4.0 (14)	5.9 (13)	1.1 (14)	2.3 (14)	(6.5±1.5) (13)	(2.4±0.3) (13)	(7.0±1.4) (13)
OH	2.6 (14)	—	1.1 (14)	6.4 (13)	—	8.4 (13)	1.8 (14)	—	(4.8±0.5) (13)	—
CS	1.4 (13)	—	5.1 (13)	1.2 (14)	—	1.1 (13)	7.5 (13)	(0.4–8) (13)	(0.7–5) (12)	(0.4–7) (13)
CN	6.5 (12)	1.1 (13)	2.5 (13)	7.9 (13)	2.0 (13)	9.7 (12)	3.5 (13)	(1.2±0.2) (13)	(2.9±0.3) (12)	(5.5±0.6) (13)
HCN	8.9 (10)	—	2.5 (11)	7.9 (11)	—	1.1 (11)	3.8 (11)	≤2 (13)	—	—
HCO^+	5.4 (11)	—	2.2 (11)	1.4 (11)	—	1.6 (11)	3.8 (11)	≤2 (13)	—	—
H_2O	2.3 (13)	—	8.4 (12)	5.2 (12)	—	6.1 (12)	1.5 (13)	—	<2.2 (13)	—
C_2H	1.3 (13)	—	4.7 (13)	9.3 (13)	—	2.2 (13)	5.8 (13)	—	—	—
C_3H_2	2.0 (9)	—	2.5 (10)	1.7 (11)	—	6.4 (9)	3.4 (10)	≤2 (13)	<5.6 (11)	—
e/H_2	1.1 (−4)	5.6 (−5)	7.1 (−5)	3.5 (−5)	1.6 (−5)	1.0 (−4)	4.3 (−5)			
C I 609 μm[d]	1.1 (−8)	1.3 (−8)	2.3 (−8)	6.6 (−8)	1.9 (−8)	1.5 (−8)	3.4 (−8)			
C I 370 μm[d]	1.3 (−8)	1.5 (−8)	1.9 (−8)	6.6 (−8)	2.0 (−8)	1.2 (−8)	3.4 (−8)			
C II 158 μm[d]	1.6 (−6)	1.5 (−6)	4.5 (−7)	6.3 (−7)	2.1 (−7)	5.0 (−7)	1.0 (−6)			
A_V(mag)	1.0	1.0	1.0	1.0	1.0	1.0	1.3	1.0	0.8	3.3

[a] In cm^{-2}

[b] All models have $\delta_O = 0.5$, $\delta_N = 0.7$, and use grain model 2, unless otherwise indicated. The adopted cosmic ray ionization rate $\zeta_0 = 5\,10^{-17}\,s^{-1}$, the $C^+ + H_2$ radiative association rate $k_{ra} = 5\,10^{-16}\,cm^3\,s^{-1}$, and the branching ratio to OH in the H_3O^+ dissociative recombination is 0.65. The abundances of other heavy elements are similar to those inferred for the ζ Oph cloud by Lepp et al. (1988)

[c] The steep-rising extinction curve as observed toward HD 204827 is adopted in the calculation of the abundances of the tabulated species

[d] In ergs $s^{-1}\,cm^{-2}\,sr^{-1}$

Table 7. Millimeter emission line searches

Molecule	Frequency (GHz)	$(\Delta\alpha, \Delta\delta)$ (arcmin)	t_{int} (min)	T_A^* (mK)
C_3H_2	85.339	(−32, 2)	110	≤30
HCN	88.631	(−32, 2)	96	≤35
HCO^+	89.188	(−7.3, −10)	190	≤25
CS	97.980	(0, 0)	120	≤25
		(−7.3, −10)	60	≤40
$C^{18}O$	109.782	(−8, −10)	95	≈70[a]
CN	113.5	(0, 0)	184	≤27
		(−8, −10)	70	≤40
		(−31.7, 1.8)	37	≤50

[a] $\int T_A^* dV = 0.06$ K km s^{-1}, $V_{LSR} = -6.04$ km s^{-1}, $\Delta V = 0.86$ km s^{-1}

The ^{13}CO column density derived in a similar manner is $(2\pm1)\,10^{14}$ cm^{-2}, virtually independent of the physical conditions in the cloud. Thus, $^{13}CO/H_2 \approx 2\,10^{-7}$, far lower than the value of $2\,10^{-6}$ assumed in Dickman's (1978) analysis. The $^{12}CO/^{13}CO$ column density ratio is about 35 ± 10.

If a similar analysis is applied to the measured CO line strengths at the (−8, −10) position in region A, the column densities are more uncertain because of the higher optical depths. The derived ^{12}CO column density is $(1.5\pm1)\,10^{16}$ cm^{-2}, whereas the ^{13}CO column density is $(1.5\pm1)\,10^{15}$ cm^{-2}. Thus, the $^{12}CO/^{13}CO$ ratio may be only 10 at this position, although the uncertainty in the ^{12}CO column density allows a large range. $C^{18}O$ was detected very weakly at this position as well with $T_A^* \approx 0.07\pm0.04$ K. The inferred $C^{18}O$ column density is $(7\pm4)\,10^{13}$ cm^{-2} so that $^{13}CO/C^{18}O \approx 20^{+30}_{-10}$ and $^{12}CO/C^{18}O \approx 200^{+300}_{-100}$. Because of the weakness of the ^{13}CO line, $C^{18}O$ was not sought toward HD 210121 itself.

CS was detected toward HD 210121 by Drdla et al. (1989) at the level $T_A^* = 0.036$ K. However, sensitive searches using the SEST telescope did not reveal a line at the level $T_A^* \approx 0.025$ K (2σ limit) at the stellar position, nor at a 1′ offset position, nor at the position (−8, −10) in region A (see Table 7). Similarly, a spectrum at the stellar position with the IRAM 30 m telescope did not exhibit any line at the 0.03 K rms level. The CS observations at Bell Labs were slightly more sensitive, however, in particular if we take into account that the SEST temperature scale may be systematically low. This comparison between the various telescopes emphasizes the difficulties associated with detecting weak lines in clouds of low total column density.

Searches for the HCO^+ ion are interesting, because its abundance provides limits on the electron density in the cloud as well (Crutcher 1985). The ion was detected in the translucent cloud toward HD 29647, which has $A_V \approx 3$ mag. However, it was not seen toward the peak position in region A at the level $T_A^* = 25$ mK. Statistical equilibrium calculations for $T = 15$–20 K and $n = 200$–1000 cm^{-3}, including excitation by electrons, suggest upper limits on the HCO^+ column density of (0.4–2.5) 10^{12} cm^{-2}.

C_3H_2 has been found to have a quite high abundance in translucent clouds with column densities of a few times 10^{12} cm^{-2} (Cox et al. 1988). The molecule has also been seen in some high-latitude clouds by Turner et al. (1989). On the other hand, C_3H_2 was not detected in the classical diffuse cloud toward ζ Oph (Madden et al. 1989). Most previous searches for C_3H_2 have involved the low-lying 1_{10}–1_{01} transition at 18 GHz in the ortho-ladder and the 2_{20}–1_{11} transition at 21 GHz in the para-ladder. We searched for the higher-lying 2_{12}–1_{01} line at 85.339 GHz in the ortho-ladder toward the peak position in region B, but did not detect any emission at the level $T_A^* = 30$ mK. This implies that the C_3H_2 column density is less than about (0.3–2) 10^{13} cm^{-2}.

Finally, although CN was not detected toward the peak position in region B, a hint of HCN was found at the peak location (−32, 2) with $T_A^* \approx 35$ mK for the strongest $1\rightarrow0$ $F=2\rightarrow1$ hyperfine component. This possible detection suggests an HCN column density of about (0.4–2) 10^{13} cm^{-2}, comparable to that of CN toward the star.

4.2. Models

4.2.1. Homogeneous models

Table 6 summarizes the observed column densities toward HD 210121. When upper limits were obtained only toward offset positions, it is assumed that the same limits apply to the line of sight toward the star itself. For comparison, the table includes the observed column densities in the classical diffuse cloud toward ζ Oph, and in the translucent cloud toward HD 169454 (Jannuzi et al. 1988). It appears that the column densities in the high-latitude cloud toward HD 210121 fall nicely in the middle between those found in diffuse clouds and in the somewhat thicker translucent clouds, and do not appear abnormal. The CO abundance increases more steeply with total H_2 column density than do the abundances of other molecules, but this is readily understood in terms of theoretical models which treat the photodissociation of CO in detail (van Dishoeck & Black 1988; Viala et al. 1988). The clouds listed in Table 6 lie in the regime where the CO abundance changes rapidly with total column density (or total visual extinction), because atomic carbon is converted into CO in the center (see Fig. 8 of van Dishoeck & Black 1988). The exact location of this transition depends sensitively on the physical parameters of the cloud, such as density and strength of the incident radiation field, but it occurs typically between $A_V \approx 1$–3 mag.

In order to illustrate this point quantitatively for the HD 210121 cloud, we constructed five theoretical models along the lines described by van Dishoeck & Black (1986, 1988, 1989) and van Dishoeck (1990). Model 1 has a low density, $n_H = n(H) + 2n(H_2) = 500$ cm^{-3}, consistent with the lower limit on the density found from the C_2 observations. In order to obtain a large CO column density at such low visual extinctions, the incident ultraviolet radiation field must be somewhat lower, $I_{UV} = 0.5$, than the standard value of Draine (1978), for which the scaling factor $I_{UV} = 1$. Model 2 has the same scaling factor $I_{UV} = 0.5$, but a somewhat higher density, $n_H = 1500$ cm^{-3}, while model 3 has an even higher density, $n_H = 5000$ cm^{-3}, consistent with the CO excitation analysis. Model 4 is the same as Model 2, except that the radiation field is increased to $I_{UV} = 1$. The temperature is low in the center of the models, $T \approx 15$–20 K, but varies with depth and is somewhat higher at the edge, $T_{edge} \approx 25$–50 K. The results also depend on the adopted grain model and extinction curve. The standard calculation uses grain model 2 of Roberge et al. (1981), but the table includes results for more steeply rising extinction curves, such as observed for example toward HD 204827 (see van Dishoeck & Black 1989 for more details). The

H_2 column density is kept at $N(H_2) = 8\,10^{20}$ cm^{-2} in models 1–4, but is increased to $N(H_2) = 1\,10^{21}$ cm^{-2} in model 5. The adopted carbon depletion factor and the other molecular parameters entering the chemical network are listed in the footnote to Table 6, and have been chosen mainly to reproduce the observed CH column density.

Column densities $N(^{12}CO) \approx 10^{16}$ cm^{-2} are readily obtained in these models, even at low densities. In fact, the ^{12}CO column densities in the higher density models are larger than that estimated toward the star, and are comparable to those observed toward the peak position in regions A and B. The sensitivity to total column density can be seen by comparing models 2 and 5: an increase in total H_2 column density of 20% results in an increase in CO column density of a factor of 2–3. These results raise the question whether the larger ^{12}CO antenna temperatures at positions A and B reflect larger total H_2 column densities, larger densities, or variations in incident radiation fields or grain scattering properties. The current models cannot distinguish between these possibilities; in particular, the available diagnostics of density at the offset positions are not yet reliable enough. The high density models cause problems for the other molecules, however, since they overproduce CH, C_2, CN, and CS. In particular, the failure to detect CS and CN at the offset positions argues against significantly higher densities. We also cannot exclude variations in extinction properties at the shortest wavelengths $\lambda < 1200$ Å on small scales, which could occur if the grains were destroyed at selective places by shocks, for example. The extremely steep CO emission contours in the SW part of the cloud around clump B suggest compression by some mechanism such as a shock. On the other hand, the absence of any significant velocity gradient and the weakness of the CH^+ absorption at least in the direction of the star argue against this suggestion. The simplest explanation for the observed structure in the CO map would be to assume small variations in column density from place to place. Measurements of the visual extinctions at high angular resolution throughout the cloud might help to resolve this ambiguity. An alternative view on the observed small-scale structure is presented in Sect. 4.2.2.

The $^{12}CO/^{13}CO$ column density ratio is typically 20–30 in the models if an overall carbon abundance $[^{12}C]/[^{13}C] = 45$ is adopted, consistent with the observed $^{12}CO/^{13}CO$ ratio toward HD 210121. $^{12}CO/^{13}CO$ ratios as low as 10 in the models, as are apparently observed at the peak positions in regions A and B, can only be obtained for very low temperatures $T < 15$ K. Selective photodissociation may be partly responsible for the different spatial structures of the ^{12}CO and ^{13}CO clumps, as seen e.g. in Fig. 2b. The observed ratio $^{13}CO/C^{18}O \approx 20^{+30}_{10}$ of region A compared with the overall ratios $[^{12}C]/[^{18}O] \approx 500$ or $[^{13}C]/[^{18}O] \approx 6$–11 is consistent with the models, in which $C^{18}O$ is selectively photodissociated, but not enhanced by isotope selective ion–molecule reactions, as is the case for ^{13}CO. In fact, most models give somewhat larger ratios than is observed, $^{13}CO/C^{18}O \approx 50$–80 for $[^{13}C]/[^{18}O] = 11$.

The resulting CH, C_2, CN, CS and CH^+ column densities in the models follow the same trends as found in our previous work (van Dishoeck & Black 1989). For carbon depletion factors which reproduce the observed CH and C_2 abundances, the computed column density of C_3H_2 is well below the observed upper limit. The calculated column density of HCO^+, on the other hand, is close to the observed upper limit. This ion is thought to be formed mostly from the reaction of H_3^+ with CO. In the current models, the abundance of H_3^+ is quite high, since a low rate coefficient, $k_{dr} = 1\,10^{-10}$ cm^3 s^{-1} was adopted for the dissociative recombination of H_3^+ with electrons. The rate of this reaction is still subject to considerable discussion (Adams & Smith 1989; Amano 1988; Hus et al. 1988). If a higher value $k_{dr} = 1\,10^{-7}$ cm^3 s^{-1} is used, the HCO^+ column density is lowered by factors of 5–10. The HCN column density in the models is about 2 orders of magnitude lower than that of CN, and at least a factor of 10 lower than the possible observed value in region B. The computed column densities are low because the molecule is rapidly photodissociated (van Dishoeck 1988). Further confirmation of the possible detection of HCN at this position is warranted.

The column densities of a number of other species are included in the table. Observations of the C and C^+ column densities toward HD 210121 with the high-resolution spectrograph on the Hubble Space Telescope would provide direct tests of the adopted carbon abundance in the models. In addition, the excitation of the atomic fine-structure levels provides independent diagnostics of the density in the cloud. Measurements of the submillimetre and far-infrared lines might give insight on possible gradients in the gas-phase carbon abundance across the cloud. Predictions of the intensities of these lines are included in Table 6. It should be noted, however, that they are very sensitive to the adopted temperature structure in the models. Observations of absorption lines of OH and possibly H_2O might also provide significant tests of the models: a large OH column density argues in favor of a low incident radiation field and a low carbon abundance. Millimetre lines of molecules like C_2H may be detectable in the cloud.

In summary, the observed column densities can be reproduced in models with densities ranging from 500 to 5000 cm^{-3} and a low incident radiation field. For these parameters, carbon and sulfur need to be depleted significantly from the gas phase to prevent overproduction of CH, C_2 and CS, especially at the higher densities. The relatively low $^{12}CO/^{13}CO$ column density ratio argues in favor of a low temperature throughout the cloud, consistent with the C_2 excitation analysis. Several diagnostic observational tests of the models are suggested. A direct measurement of the ultraviolet extinction curve toward HD 210121 would be very useful as well.

4.2.2. Inhomogeneous models

There has been growing evidence in recent years that molecular clouds exhibit spatial structure on all scales down to the best angular resolution (e.g. Pérault et al. 1985; Falgarone & Pérault 1988, hereafter FP), with significant density variations from place to place (Falgarone et al. 1991, hereafter FPW). It is therefore warranted to investigate the influence that such structure would have on our analysis. Most of the evidence for the density variation comes from high-resolution CO maps of selected areas of clouds with low total H_2 column density, only somewhat thicker than the cloud we have studied here. Channel maps, especially of the ^{13}CO emission, reveal isolated "cells" in (l, b, v) space, which have typical filling factors of 25–50%. Both the $^{12}CO/^{13}CO$ intensity ratio and the relative strength of the CO $J = 3 \rightarrow 2$ emission suggest densities of 10^4 cm^{-3} or more in such cells.

A similar analysis could be applied to the data presented here, in particular to the $3' \times 3'$ region around HD 210121, which has been fully sampled in the ^{12}CO $1 \rightarrow 0$ line (see Figs. 7 and 8).

However, one important difference is that the region around HD 210121 is of even lower column density than those studied by FP and FPW: the ^{12}CO antenna temperatures are typically lower by a factor 2, and those of ^{13}CO, by more than an order of magnitude. As a result, mapping of ^{13}CO in this region was not possible. The ^{12}CO channel maps presented in Fig. 8 reveal some structure; the most prominent feature is a "cell" of about 60″ in diameter (0.04 pc) at $V_{LSR} = -6$ to -5.5 km s^{-1} centered at the position of the star, which has an areal covering factor of about 30%. Over this area, the ^{13}CO emission stays low, $T_A^* \approx 0.07$ K. In order to constrain the density, FP and FPW subsequently make the assumption that the CO column density of order $7\ 10^{15}$ cm^{-2} (cf. Sect. 4.2.1) builds up along a line-of-sight length L comparable to the projected diameter of the observed structure. The same arguments applied to our cloud then lead to an estimate of the average H_2 density over L of $n \approx (N(CO)/L) \times (CO/H_2)^{-1}$ ≈ 5000 cm^{-3} for $CO/H_2 \approx 10^{-5}$, which is reasonably consistent with that derived from the CO $1 \rightarrow 0/3 \rightarrow 2$ ratio. However, since similar structure is expected to exist on even smaller scales, FPW would caution that this density should be regarded only as a lower limit. On the other hand, we note that a higher local abundance in the region of peak CO emission of 10^{-4} would imply a smaller local density of only 500 cm^{-3}.

Clearly, densities of 10^4 cm^{-3} or more toward the star are inconsistent with the excitation analysis of the C_2 and CN absorption lines presented in Sect. 3.6. One possible explanation for this discrepancy could be that the "pencil beam" line of sight toward the star missed the densest clump(s) responsible for the small scale structure and the $3 \rightarrow 2$ emission. In fact, this explanation would have to hold for many more lines of sight for which absorption lines have been obtained, since the densities derived from the C_2 excitation are often less than 1000 cm^{-3}. This would imply that the dense clumps have a quite low filling factor, certainly much less than 30%.

Because the CO map in Figs. 7 and 8 at the central velocity is rather homogeneous and because the $^{12}CO/^{13}CO$ ratio is high, it appears more likely that most of the ^{12}CO $1 \rightarrow 0$ emission around the star arises from a more widespread, low density component. FPW assert that such a component should be present, but that it will not contribute much to the $2 \rightarrow 1$ and $3 \rightarrow 2$ emission. It is difficult to determine a filling factor for this more dilute gas from the observations. However, even a filling factor of 30% would increase the CO column density by only a factor 3 (but averaged over a smaller volume). The resulting $N(CO) \approx$ a few times 10^{16} cm^{-2} would still imply that most of the carbon is in atomic form in this cloud.

Unfortunately, it is not yet possible to make any more detailed chemical models of such inhomogeneous clouds, because the mass fraction in each of the components (dense clumps vs. low-density widespread material) is not yet known (cf. FPW). Moreover, the ultraviolet radiation field penetrates such "clumpy" structures in a complicated way (cf. Boissé 1990). Some idea as to how the abundances of molecules like CH, C_2, CN and CO may change can be obtained from the inhomogeneous models presented by van Dishoeck et al. (1991). One conclusion from these models is that any small, very dense clump along the line of sight can easily dominate the integrated abundances (i.e. column densities) of all these molecules. The way in which the radiation field enters the cloud (e.g. one-sided vs. two-sided) was also found to have strong effects. Since the CH, C_2 and CN abundances do not appear "abnormal" toward HD 210121 compared with low density diffuse clouds, it appears unlikely that such a dense clump is present along the line of sight to the star. Finally, we note that even though some of these dense clumps may be isolated entities in velocity space, they can shield the CO and H_2 in clumps at other velocities very effectively, since the widths of the ultraviolet lines through which the photodissociation occurs are more than 10 km s^{-1}. Thus, the observed CO column density does not necessarily have to build up over just one such "cell".

In summary, although small-scale structure may be present in these clouds of low column density, the effect it has on the chemistry is difficult to assess until we have a better understanding of the small scale structure of the interstellar gas. It is argued that for the case of the HD 210121 clouds, the effects are likely to be small and are not expected to change any of our main conclusions of Sect. 4.2.1.

5. Discussion

The SEST observations of the molecular cloud toward HD 210121 reveal its highly fragmentary spatial structure on scales of a few pc. Individual, localized regions with spatial dimensions of a few 0.1 pc are discernible. The strongest CO $J = 1 \rightarrow 0$ emission is concentrated in an elliptical shell centered approximately on $\alpha(1950) = 22^h04^m30^s$ and $\delta(1950) = -3°41'$. Only weak emission fills the central part of this apparent shell, although the dynamic range between the lowest contour and the peak emission in Fig. 1a is only a factor of 5–6. The overall shell-like morphology raises intriguing questions about the origin of the cloud and its evolutionary state. The uniformly narrow line profiles and the complete lack of any significant velocity gradient argue against an energetic explosion as the source of the shell structure. Moreover, there is no prominent source of X-rays, infrared radiation, or radio continuum emission coincident with the apparent center of symmetry of the cloud, nor is there any conspicuous star or compact nebula to be found there. From the appearance of the CO map (Fig. 1a), approximately 1/3 of the *projected* area is covered by readily detected emission, which corresponds to a fraction 0.19 of the corresponding spherical volume. The "unfilled" fractional volume (0.81) is only slightly less than the fraction of the total virial mass that is not traced by detectable CO (cf. Table 3). As we have emphasized, the *apparent structure* is delicately sensitive to column density of observable CO but does not necessarily reflect large density contrasts; in any case, the dynamic range of the map is not large. If, for example, the original total mass of the cloud had been equal to the inferred virial mass, $\approx 670 M_\odot$, perhaps $180 M_\odot$ could remain in atomic form and even expand gradually through the holes between slightly denser molecular concentrations. If so, then a localized atomic cloud should be recognizable through H I 21 cm line emission. There is indeed a feature at the correct velocity and position in the survey of Heiles & Habing (1974), but the beam size of the telescope used for their measurements is comparable to the angular size of the entire molecular cloud. A 21 cm map of higher resolution would help to put a measure on the otherwise unseen atomic mass, its extent, and its velocity dispersion, and this work is in progress (Stark et al. 1992 in preparation). With such information it would be possible to make a more reliable assessment of the total pressure in and around the cloud. Overall the molecular component of the entire cloud appears not far out of virial balance. That the individual molecular concentrations appear to have masses much smaller than virial masses computed

from local velocity dispersions (Sect. 3.5 and Table 3) may be as illusory as the apparent structure itself, if that structure results from rather small density or column density contrasts. It is an essential fact about this cloud that the local velocity dispersions are quite similar to the dispersion across the entire cloud: for all its *apparent small-scale structure*, it is a rather quiescent system.

The linear extents of the clumps in the HD 210121 cloud are smaller than the Jeans length of $\lambda_J = \sqrt{\pi KT/\mu m_H Gn} \approx 0.6$ pc for a gas at kinetic temperature of $T = 15$ K and density of $n = 1000\ \mathrm{cm}^{-3}$. Only at a significantly higher average density of the order of $n \approx 10^{4.6}$ would $\lambda_J \approx 0.1$ pc. Fragmentation at scales smaller than the Jeans length could occur in rotating clouds, but there is no obvious evidence of systematic rotation. The second velocity component seen in region D is the only striking anomaly in the kinematics of the cloud. It could arise, for example, along a line of sight through both front and back sides of a shell that has a slight expansion. The additional velocity component at $V = +5\ \mathrm{km\,s}^{-1}$ in the Na I D lines toward HD 210121 also appears in the H I 21 cm emission and it is not yet clear to which extent this component is related to the molecular cloud.

6. Conclusions

Although small-scale structure is commonly observed in CO maps of high-latitude and translucent molecular clouds, the interpretation of such structure is not trivial. The analysis of the HD 210121 cloud demonstrates that small fluctuations of order 20–50% in H_2 column density, density, ultraviolet radiation field or grain scattering properties can produce large variations of CO abundance and column density in these clouds where carbon is just being transformed into CO. Thus, the apparent structure in CO maps may be greatly exaggerated compared with the true fluctuations in physical parameters. As a general conclusion, it will be very difficult to isolate the physical quantity that is primarily responsible for the observed structure.

The HD 210121 cloud fits neatly into the middle of the whole scala of translucent and high-latitude clouds that have been observed in recent years. It has slightly larger molecular column densities than found in the classical diffuse clouds, but smaller column densities than measured in translucent clouds such as those toward HD 169454 and HD 29647. It is clearly less thick than high-latitude clouds such as MBM 12, which have been mapped in detail even in ^{13}CO (Pound et al. 1990): the ^{13}CO emission in the HD 210121 cloud is quite weak and C^{18}O is barely detectable. On the other hand, the cloud toward HD 210121 is probably thicker than the majority of clouds listed by Désert et al. (1988). Its chemical abundances are consistent with those found in other translucent clouds.

The HD 210121 cloud is one of the best-studied high-latitude cloud to date in terms of physical structure and chemical abundances, owing to the availability of complementary optical and millimetre data. Similar studies of high-latitude clouds over a range of thickness are warranted, and might eventually reveal the true origin of the small-scale structure in these clouds.

Acknowledgments. This research was supported by the Netherlands Organization for Scientific Research, NWO. J.H.B. also acknowledges support from NASA through grant NAGW-763 to the University of Arizona. R.G. is grateful to R. Booth for providing an ESO fellowship at SEST, and to L.E.B. Johansson and L.Å. Nyman for sharing a large part of SEST maintenance time for the observations. The authors thank E. Falgarone for useful discussions on the small-scale structure of the clouds. The anonymous referee and the editor, J. Lequeux, provided significant comments on the manuscript.

References

Adams N.G., Smith D., 1989, in: Mitchell J.B.A., Guberman S.L. (eds.) Dissociative Recombination: Theory, Experiments and Applications. World Scientific Publishing, Singapore, p. 124
Amano T., 1988, ApJ 329, L121
Black J.H., van Dishoeck E.F., 1988, ApJ 331, 986
Black J.H., van Dishoeck E.F., 1991a, ApJ 369, L9
Black J.H., van Dishoeck E.F., 1991b, in: Falgarone E., Boulanger F., Duvert G. (eds.) IAU Symposium 147, Kluwer, Dordrecht, p. 139
Blitz L., Bazell D., Désert F.X., 1990, ApJ 352, L13
Blitz L., Magnani M., Mundy L., 1984, ApJ 282, L9
Blitz L., Magnani M., Wandel A., 1988, ApJ 331, L127
Bloemen J.B.G.M., Strong A.W., Blitz L., et al., 1986, A&A 154, 25
Boissé P., 1990, A&A 228, 483
Booth R.S., Delgado G., Hagström M., et al., 1989, A&A 216, 315
Cox P., Güsten R., Henkel C., 1988, A&A 206, 108
Crutcher R.M., 1985, ApJ 288, 604
Danks A.C., Federman S.R., Lambert D.L., 1984, A&A 130, 62
Dekker H., Delabre B., D'Odorico S., et al., 1986, Messenger 43, 27
Désert F.X., Bazell D., Boulanger F., 1988, ApJ 334, 815
de Vries C.P., Le Poole R., 1985, A&A 145, L7
de Vries C.P., van Dishoeck E.F., 1988, A&A 203, L23
de Vries H.W., Heithausen A., Thaddeus, P., 1987, ApJ 319, 723
Dickman R.L., 1978, ApJS 37, 407
Draine B.T., 1978, ApJS 36, 595
Drdla K., Knapp G.R., van Dishoeck E.F., 1989, ApJ 345, 815
Falgarone E., Pérault M., 1988, A&A 205, L1
Falgarone E, Phillips T.G., 1990, ApJ 359, 344
Falgarone E., Phillips T.G., Walker C., 1991, ApJ 378, 186
Goerigk W., Mebold U., Reif K., Kalberla P.M.W., Velden L., 1983, A&A 120, 63
Gredel R., Münch G., 1986, A&A 154, 336
Gredel R., van Dishoeck E.F., Black J.H., 1991, A&A 251, 625
Heiles C., Habing H.J., 1974, A&AS 14, 1
Heithausen A., Mebold U., de Vries H.W., 1987, A&A 179, 263
Herbstmeier U., Rohlfs R., Mebold U., 1989, in: Winnewisser G., Armstrong J.T. (eds.) The Physics and Chemistry of Interstellar Molecular Clouds. Springer, Heidelberg, p. 195
Hobbs L.M., Blitz L., Magnani L., 1986, ApJ 306, L109
Hobbs L.M., Blitz L., Penprase B.E., Magnani L., Welty D.E., 1988, ApJ 327, 356
Hus H., Youssif F., Sen A., Mitchell J.B.A., 1988, Phys. Rev. A 38, 658
Jannuzi B.T., Black J.H., Lada C.J., van Dishoeck E.F., 1988, ApJ 332, 995
Keto E.R., Myers P.C., 1986, ApJ 304, 466
Knapp G.R., Bowers P.F., 1988, ApJ 331, 974
Kutner M.L., Ulich B.L., 1981, ApJ 250, 350
Lada E.A., Blitz L., 1988, ApJ 326, L69
Langer W.D., Glassgold A.E., Wilson R.W., 1987, ApJ 322, 450
Lepp S., Dalgarno A., van Dishoeck E.F., Black J.H., 1988, ApJ 329, 418

Lynds B., 1962, ApJS 7, 1
Madden S.C., Irvine W.M., Matthews H.E., Friberg P., Swade D.A., 1989, AJ 97, 1403
Magnani L., de Vries C.P., 1986, A&A 168, 271
Magnani L., Siskind L., 1990, ApJ 359, 355
Magnani L., Blitz L., Mundy L., 1985, ApJ 295, 402
Magnani L., Blitz L., Wouterloot J.G.A., 1988, ApJ 326, 909
Magnani L., Carpenter J.M., Blitz L., Kassim N.E., Nath B.B., 1990, ApJS 73, 747
Magnani L., Lada E.A., Sandell G., Blitz L., 1989, ApJ 339, 244
Mather J., Cheng E.S., Eplee R.E., et al., 1990, ApJ 354, L37
Mattila K., 1986, A&A 160, 157
Mebold U., Cernicharo J., Velden L., et al., 1985, A&A 151, 427
Mebold U., Heithausen A., Reif K., 1987, A&A 180, 213
Penprase B.E., Blades J.C., Danks A.C., Crane P., 1990, ApJ 365, 241
Pérault M., Falgarone E., Puget J.L., 1985, A&A 152, 371
Polk K.S., Knapp G.R., Stark A.A., Wilson R.W., 1988, ApJ 332, 432
Pound M.W., Bania T.M., Wilson R.W., 1990, ApJ 351, 165
Roberge W.G., Dalgarno A., Flannery B.P., 1981, ApJ 243, 817
Solomon P.M., Scoville N.Z., Sanders D.B., 1979, ApJ 232, L89
Stacy J.G., Myers P.C., de Vries H.W., 1989, in: Winnewisser G., Armstrong J.T. (eds.) The Physics and Chemistry of Interstellar Molecular Clouds, Springer, Heidelberg, p. 117
Turner B.E., Rickard L.J., Xu L.-P., 1989, ApJ 344, 292
van Dishoeck E.F., 1988, in: Millar T.J., Williams D.A. (eds.) Rate Coefficients in Astrochemistry, Kluwer, Dordrecht, p. 49
van Dishoeck E.F., 1990, in: Blitz L. (ed.) The Evolution of the Interstellar Medium, A.S.P. Conference series nr. 12. Astronomical Society of the Pacific, San Francisco, p. 207
van Dishoeck E.F., Black J.H., 1982, ApJ 258, 533
van Dishoeck E.F., Black J.H., 1986, ApJS 62, 109
van Dishoeck E.F., Black J.H., 1988, ApJ 334, 771
van Dishoeck E.F., Black J.H., 1989, ApJ 340, 273
van Dishoeck E.F., de Zeeuw T., 1984, MNRAS 206, 383
van Dishoeck E.F., Black J.H., Phillips T.G., Gredel R., 1991, ApJ 366, 141
Viala Y.P., Letzelter C., Eidelsberg M., Rostas F., 1988, A&A 193, 265
Welty D.E., Hobbs L.M., Blitz L., Penprase B.E., 1989, ApJ 346, 232
Weiland J.L., Blitz L., Dwek E., et al., 1986, ApJ 306, L101
Zensen W., 1984, Ph.D. Dissertation, University of Cologne, Cologne